Review

Morphological Dependence of Metal Oxide Photocatalysts for Dye Degradation

Ahmed H. Naggar [1,*], Abdelaal S. A. Ahmed [2], Tarek A. Seaf El-Nasr [3], N. F. Alotaibi [3], Kwok Feng Chong [4] and Gomaa A. M. Ali [2,5,6,*]

[1] Department of Chemistry, College of Science and Arts, Jouf University, Al Qurayyat 75911, Saudi Arabia
[2] Chemistry Department, Faculty of Science, Al-Azhar University, Assiut 71524, Egypt; abdelaalsaiyd@azhar.edu.eg
[3] Department of Chemistry, College of Science and Arts, Jouf University, Sakaka 2014, Saudi Arabia; taahmed@ju.edu.sa (T.A.S.E.-N.); nfotaibi@ju.edu.sa (N.F.A.)
[4] Faculty of Industrial Sciences & Technology, Universiti Malaysia Pahang Al-Sultan Abdullah, Gambang, Kuantan 26300, Malaysia; ckfeng@umpsa.edu.my
[5] Faculty of Advanced Basic Science, Galala University, Suez 43511, Egypt
[6] Faculty of Industry and Energy Technology, New Assiut Technological University, Assiut 71684, Egypt
* Correspondence: ahayoub@ju.edu.sa (A.H.N.); gomaasanad@azhar.edu.eg (G.A.M.A.)

Abstract: There is no doubt that organic dyes currently play an indispensable role in our daily life; they are used in products such as furniture, textiles, and leather accessories. However, the main problems related to the widespread use of these dyes are their toxicity and non-biodegradable nature, which mainly are responsible for various environmental risks and threaten human life. Therefore, the elimination of these toxic materials from aqueous media is highly recommended to save freshwater resources, as well as our health and environment. Heterogeneous photocatalysis is a potential technique for dye degradation, in which a photocatalyst is used to absorb light (UV or visible) and produce electron–hole pairs that enable the reaction participants to undergo chemical changes. In the past, various metal oxides have been successfully applied as promising photocatalysts for the degradation of dyes and various organic pollutants due to their wide bandgap, optical, and electronic properties, in addition to their low cost, high abundance, and chemical stability in aqueous solutions. Various parameters play critical roles in the total performance of the photocatalyst during the photocatalytic degradation of dyes, including morphology, which is a critical factor in the overall degradation process. In our article, the recent progress on the morphological dependence of photocatalysts will be reviewed.

Keywords: organic dyes; wastewater treatment; photocatalyst; photocatalytic degradation; metal oxides; morphology

1. Introduction

Due to the growth of societies and the speeding up of industry over the last few decades, environmental pollution is considered the biggest challenge facing our societies [1]. Almost all activities of humans to produce commodities and services lead to the creation of environmental contaminants. These pollutants cause harm to the health of people, plants, animals, and microbes when they are discharged into the air, water, and soil [2]. Since humans depend on the creation and enhancement of commodities and services to survive on earth, these practices cannot be completely abandoned [2]. Major contributors toward aquatic pollution include industrial dyes, which are the greatest class of organic pollutants [3,4]. Due to their intricate chemical compositions, the majority of synthetic dyes are poisonous and extremely durable. Currently, synthetic dyes as organic compounds or mixtures are widely utilized in the leather, pharmaceutical, food, cosmetic, color photography, paper printing, textile dyeing, and textile dyeing industries [5–8].

The last two decades have seen a dramatic rise in public understanding of the toxic and cancer-causing effects of many pollutants that were previously not thought to be dangerous [2]. Some man-made chemicals can linger in the environment for a very long time without degrading, in contrast to naturally occurring compounds that break down immediately. These substances, which include pesticides, organochlorines, polychlorinated biphenyls, synthetic polymers, and synthetic dyes, are regarded as the main environmental contaminants [9]. Most dyes are organic, multidimensional compounds with the property of adhering to various surfaces, including fabrics, leathers, and others. The paper, textile, dyestuff, and distilling industries release highly colored wastewaters [10]. By increasing the demand for dyes, a larger amount of water is polluted [11,12]. As reported by Couto et al., in traditional dying processes, each 1 kg of textile materials required about 100 L of water to obtain the final product [5]. As per O'Neill et al., not every type of dye adheres to fabric, and their discharge in wastewater varies. Basic dyes may lose up to 2% while reactive dyes can lose up to 50%, resulting in the contamination of surface and ground waters in the dyeing industries [13].

It has been reported that each year about 280,000 tons of textile dyes are released into industrial wastewater by the textile industry [14]. In general, it is thought that throughout the industrial processes, roughly 12% of the total generated synthetic dyes, including methyl orange (MO), methyl red (MR), methylene blue (MB), rhodamine B (RhB), remazol brilliant blue (RB), congo red (CR), and many others, are lost [3,15]. Additionally, 15–20% of global dye production is wasted during the dying process and released into water without additional treatment, resulting in significant environmental damage [16]. The presence of color in dye effluents serves as a clear indicator that water is contaminated since it is easier to see, and the discharge of these strongly colored effluents can directly impact the receiving waterways [17]. Even a very small concentration (1 mg L^{-1}) of synthetic dyes in water can generate color and create an unfavorable concentration for ingestion, and also can significantly harm the environment and pose substantial health risks [18]. When utilizing the untreated dyeing effluents in agriculture purposes, both the environment and human health are badly affected [19]. In light of the harmful and cancer-causing properties associated with dyes, and considering that numerous dyes are known carcinogens, significant recent endeavors have been directed towards regulating the release of dyes into the environment [20,21]. The remediation of dye wastewaters can be accomplished using various techniques. A variety of procedures are involved, comprising biological and microbiological methods, along with physicochemical techniques such as adsorption, chemical oxidation, precipitation, coagulation, filtration, electrolysis, and photodegradation [22]. Based on its suitability, each strategy can be used to target a certain class of toxins and offers advantages of its own. Despite their usefulness, physicochemical techniques often suffer from several limitations, including high costs, low efficiency, limited flexibility, susceptibility to interference from other wastewater constituents, and the challenge of managing the waste generated [18].

Therefore, it is crucial to develop affordable, effective, and environmentally friendly methods to reduce the amount of dye in wastewater [5]. Advanced oxidation processes (AOPs) can be used for treating most industrial effluents. Among the numerous AOPs that are recognized, photocatalytic degradation has emerged as a promising method for destroying organic substances [23,24]. The photodegradation process of dyes involves oxidizing large dye molecules into smaller ones such as water, carbon dioxide, and other byproducts. Compared to other AOPs, photocatalytic degradation is more successful since semiconductors are less expensive and can easily mineralize a variety of organic molecules. The materials used as effective photocatalysts should have an appropriate energy band gap, appropriate morphology, high surface area, long term stability, and considerable recycling ability [25,26]. Due to the high surface-to-volume ratio of nanomaterials, more surface area is available for redox reactions. In recent years, metal oxides have garnered significant interest in environmental remediation due to their ability to generate charge carriers upon activation by sufficient energy [27]. Numerous metal oxide nanoparticles

have been employed as photocatalysts in the past, including zinc oxide (ZnO), titanium dioxide (TiO_2), copper oxide (CuO), nickel oxide (NiO), and tungsten oxide (WO_3). This is a result of their potential optical, chemical, and physical capabilities, including their distinct electronic structures, abilities to absorb light, and capacities for charge transport [28]. The composition, size, doping, and shape of metal oxides are only a few of the variables that might influence their photocatalytic activity. These factors are all crucial for photocatalytic activity [29–32]. This study mainly reviews the recent progress on the morphologically dependent photocatalytic activity of the metal oxides toward degradation of organic dyes from aqueous solutions. From the metal oxides, TiO_2, ZnO, CuO, NiO, and WO_3, with various morphologies, will be presented. To provide a big picture, our article starts with an introduction that outlines the dye classifications and their environmental problems. Additionally, this article outlines the principle of the photocatalytic process and the different photocatalytic reaction mechanisms.

In addition, this review presents a comprehensive study of the recent progress made in the field of the morphological dependence of photocatalysts for the photocatalytic degradation of organic dyes. It discusses the latest developments in the synthesis and characterization of metal oxide photocatalysts with tailored morphologies. Furthermore, it analyzes the underlying mechanisms governing morphology-induced effects and provides insights into the prospects and challenges in this research area.

According to publication records during the last decade, there were about 77,214 publications on photocatalysis. The research output on photocatalysis has continued growing with time, with 4155 and 10,550 publications in 2013 and 2023, respectively, as shown in Figure 1. Among the metal oxides, most publications investigated TiO_2, ZnO, CuO, NiO, and WO_3 materials.
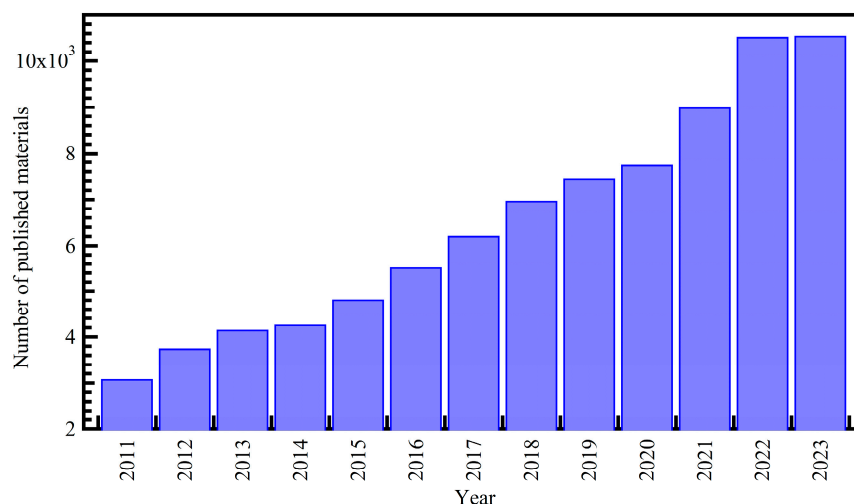

Figure 1. Distribution of the cumulative number of publications on photocatalysis per year from the Scopus database (November 2023).

2. Principles of Photocatalysis

In the last decades, the use of photocatalysis technology as a quick, affordable, and efficient way to get rid of the majority of poisonous dyes has received a lot of interest [33–35]. Photocatalysis is a field that utilizes catalysts to enhance the speed of some chemical reactions. A photocatalyst is a material capable of absorbing light, generating electron–hole pairs that enable the participants in a reaction to undergo chemical transformations [36]. The primary factor behind photocatalytic activity (PCA) is the catalyst's capability to produce electron–hole pairs, which leads to the creation of free radicals such as hydroxyl radicals (●OH). These radicals can then undergo secondary reactions. There are two primary categories of photocatalytic reactions: homogeneous photocatalysis and heterogeneous

photocatalysis. The ability of any specific photocatalytic technique to work properly depends on several characteristics, including bandgap, shape, and high surface area [37].

Since dyes are colored, it is simple to track how they change color throughout the experiment. The dye sample is exposed to UV light for a predetermined amount of time in the photocatalytic process. The variations in solution color are then measured in terms of decreasing absorbance using a spectrophotometer. The degree of discoloration (τ) is determined from the dye absorption before and after irradiation by the following relation (Equation (1)) [38].

$$\tau = 1 - \frac{A_i}{A_o} * 100 \tag{1}$$

The equation includes A_o, which denotes the absorbance of the dye solution before irradiation, and A_i, which represents the absorbance of the dye solution after irradiation.

Heterogeneous photocatalysis is an environmentally friendly, low-cost method of decontaminating organic materials. Organic contaminants can be effectively reduced through heterogeneous photocatalysis in both the atmosphere and water. The mechanism of the photocatalytic degradation of organic pollutants has been previously discussed by several groups [39,40]. Usually, sunlight in the presence of a semiconductor photocatalyst is utilized to speed up the removal of environmental contaminants and the obliteration of extremely harmful compounds [41]. The process of heterogeneous photocatalysis comprises five sequential steps: (i) transferring the reactants from the liquid phase to the catalyst surface; (ii) adsorbing the reactants onto the catalyst surface; (iii) enabling the reaction to occur in the adsorbed phase; (iv) desorbing the final product; and (v) removing the final products from the liquid phase [42].

The following steps are stated as the mechanism of dye and other organic compound degradation via photocatalysis: When the catalyst is exposed to UV light, electrons move from the valence band (VB) to the conduction band (CB), resulting in the formation of an electron–hole pair (Equation (2)) [43,44].
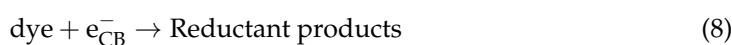
$$\text{catalyst} + \text{hv} \rightarrow \text{e}^-_{\text{CB}} + \text{h}^+_{\text{VB}} \tag{2}$$

Here, e^-_{CB} and h^+_{VB}, respectively, represent the electrons in the CB and the holes in the VB.

The produced excited substances (excitons) may travel to the catalyst surface and engage in a redox reaction with other species already there. Usually, h^+_{VB} may readily form $\bullet$OH radicals through the reaction with surface-bound H_2O molecules (Equation (3)), whereas e^-_{CB} can produce superoxide radical anions of oxygen through the reaction with O_2 (Equation (4)) [42].

$$H_2O + \text{h}^+_{\text{VB}} \rightarrow \bullet\text{OH} + H^+ \tag{3}$$

$$O_2 + \text{e}^-_{\text{CB}} \rightarrow O_2^{\bullet-} \tag{4}$$

The combination of the electron and the hole created in the first step is prevented by this reaction. The $\bullet$OH and O_2 that are created in the following equations react with the dye to create additional species, which results in the dye discoloration.

$$O_2^- + H^+ \rightarrow \bullet\text{OH}_2 \tag{5}$$

$$H_2O_2 \rightarrow 2\bullet\text{OH} \tag{6}$$

$$\bullet\text{OH} + \text{dye} \rightarrow \text{dye}_{\text{oxi}} \tag{7}$$

$$\text{dye} + \text{e}^-_{\text{CB}} \rightarrow \text{Reductant products} \tag{8}$$

Due to the presence of dissolved oxygen and water molecules, all above reactions are possible in photocatalysis. In Figure 2, the pathways of oxidative species formation in photocatalytic research are presented schematically.
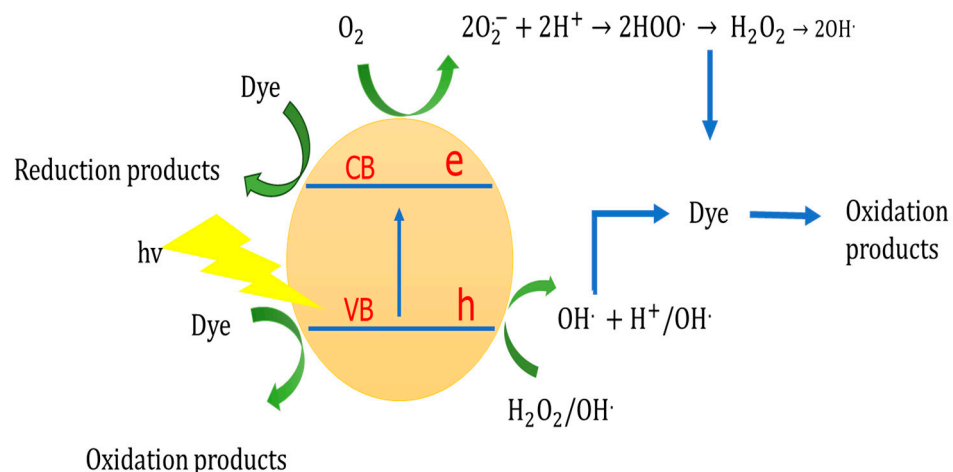
Figure 2. The mechanism of the oxidative species in heterogeneous photocatalysis. Adopted with permission from Ref. [42] Copyright 2017, Royal Society of Chemistry.

3. Mechanisms of Photocatalyzed Dye Degradation

There are two main pathways for photocatalytic reactions, as described below.

3.1. Direct Photocatalytic Pathway

There are two proposed mechanisms describing heterogeneous photocatalysis.

3.1.1. The Langmuir–Hinshelwood Model

This model is used to describe the mechanism of solid catalytic reactions [45]. As reported in the published review by Uyen N. P. Tran et al. [46], typically, the L–H mechanism model consists of four sequential steps: (1) molecules are absorbed on a catalytic surface, (2) adsorbed molecules dissociate, (3) products are produced by reactions between dissociated molecules, and (4) products are liberated to the medium. Usually, this model is used to study the heterogeneous catalytic degradation of organic pollutants in wastewater [47,48].

Based on step (1), the adsorption and desorption rate can be expressed as Equations (9) and (10).

$$r_a = k_a(1 - \theta)C_P \tag{9}$$

$$r_d = k_d\theta \tag{10}$$

Here, k_a and k_d are the adsorption and desorption rate constants, θ is a fraction of the coverage site, and C_p is the concentration of pollutant "p".

At equilibrium, $r_a = r_d$, which results in Equation (11) [49].

$$\theta = \frac{kC_p}{1 + kC_P} \tag{11}$$

k = the equilibrium constant, $k = \frac{k_a}{k_d}$

Usually, the photocatalytic degradation of an organic pollutant (P) occurs after adsorption; thus, the degradation rate is proportional to θ, as shown in Equation (12) [45].

$$r_{deg} = k_{deg}\theta = \frac{k_{deg}kC_P}{1 + kC_P} \tag{12}$$

Here, k_{deg} is the degradation rate constant.

Based on the rate law of chemical reaction, the rate of the degradation can also be expressed by the following relation:

$$r_{deg} = -\frac{dC_P}{d_t} \tag{13}$$

By combining Equations (12) and (13), L–H kinetic model can be obtained.

$$-\frac{dC_P}{d_t} = \frac{k_{deg}kC_P}{1+kC_P} \tag{14}$$

By integrating Equation (14) from $C_P = C_{P,0}$ at $t = 0$ to C_P at the interval time, t:

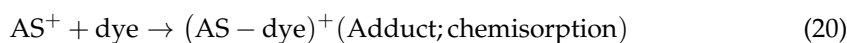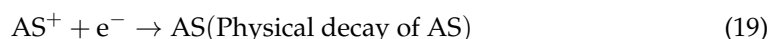$$\frac{1}{k_{deg}k}ln\frac{C_P}{C_{P,0}} + \frac{1}{k_{deg}}(C_P - C_{P,0}) = -t \tag{15}$$

$$\frac{-t}{C_P - C_{P,0}} = \frac{1}{k_{deg}} + \frac{1}{k_{deg}k}ln\left(\frac{C_P}{C_{P,0}}\right)/(C_P - C_{P,0}) \tag{16}$$

By linearly plotting the above equation, the obtained intercept and slope are $\frac{1}{k_{deg}}$ and $\frac{1}{k_{deg}k}$, respectively.

According to previous studies, the kinetic of the photocatalytic degradation is fitted well with the L–H model. For instance, Cao et al. showed that the kinetics of the photodegradation of gaseous benzene by nitrogen-doped TiO_2 (N-TiO_2) under visible light irradiation agreed with the L–H model [50]. Another study by M. Klumpp et al. [51] confirmed that the experimental data of the degradation of rhodamine B (RhB) by TiO_2 thin film also agreed with L–H model. Furthermore, Yang et al. [52] reported that the catalytic photodegradation of norfloxacin and enrofloxacin under visible light irradiation with bismuth tungstate (Bi_2WO_6) synthesized by combining ultrasonic solvothermal treatment and high-temperature calcination adopted the L–H kinetic model with a high correlation coefficient ($R^2 > 0.95$).
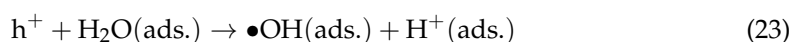
3.1.2. The Eley–Rideal Model

In this method, the holes are first photo-created, then the free charged carriers are trapped by surface flaws. The dye is then chemically altered by the active centers (AS) to produce an adduct species such as (S-dye)$^+$, which can then degrade further to produce products or recombine with electrons. The subsequent reactions depict the reaction structure [34,53]:

$$\text{Catalyst} + \text{hv} \rightarrow \text{e}^- + \text{h}^+ \text{(photogeneration of charges)} \tag{17}$$

$$\text{AS} + \text{h}^+ \rightarrow \text{AS}^+ \text{(Trapping holes by AS)} \tag{18}$$

$$\text{AS}^+ + \text{e}^- \rightarrow \text{AS} \text{(Physical decay of AS)} \tag{19}$$

$$\text{AS}^+ + \text{dye} \rightarrow (\text{AS} - \text{dye})^+ \text{(Adduct; chemisorption)} \tag{20}$$

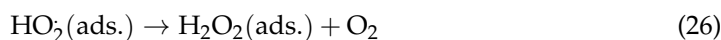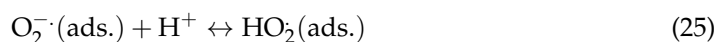$$(\text{AS} - \text{dye})^+ + \text{e}^- \rightarrow \text{AS} + \text{products} \tag{21}$$

3.2. Indirect Photocatalytic Pathway

On the surface of the catalyst, electron–hole pairs are photogenerated during this process. After that, water molecules trap the holes and create H^+ and $^\bullet OH$ radicals. The $^\bullet OH$ radicals can attack the dye to produce intermediates and finished products, or they can interact with one another to form H_2O_2. The superoxide radical, which can start a chain reaction that produces HO_2^- and H_2O_2, can also trap the electron by binding to molecules of oxygen.

The organic molecule is oxidized as a result of all these radicals being produced, creating intermediates and finished products [54]. The following equations serve as examples of the mechanism [54]:

$$TiO_2 + \text{hv} \rightarrow \text{e}^- + \text{h}^+ \tag{22}$$

$$\text{h}^+ + H_2O(\text{ads.}) \rightarrow \bullet OH(\text{ads.}) + H^+(\text{ads.}) \tag{23}$$

$$O_2 + e^- \rightarrow O_2^{-\cdot}(\text{ads.}) \tag{24}$$

$$O_2^{-\cdot}(\text{ads.}) + H^+ \leftrightarrow HO_2(\text{ads.}) \tag{25}$$

$$HO_2(\text{ads.}) \rightarrow H_2O_2(\text{ads.}) + O_2 \tag{26}$$

$$H_2O_2(\text{ads.}) \rightarrow 2HO\bullet(\text{ads.}) \tag{27}$$

$$\bullet OH + \text{dye} \rightarrow \text{intermediate} \rightarrow CO_2 + H_2O \tag{28}$$

The photodegradation efficiency and oxidation rates of a photocatalytic system are heavily dependent on various operational parameters. These parameters play a crucial role in regulating the degradation of organic molecules and include the effects of the dye concentration, catalyst dose, solution pH, light intensity, and exposure period. A comprehensive discussion of all these factors can be found in the literature [47,54].

4. Morphological Dependence of Metal Oxide Photocatalysts

Due to their capacity to produce charge carriers when stimulated with effective energy, metal oxides are generally of great interest in both environmental remediation and electronics. Numerous metal oxide nanoparticles have been utilized as photocatalysts and adhere to the fundamental principles of photocatalytic activity [28,55,56]. The first step in the photocatalytic reaction is the absorption of light, which separates charges and creates (h^+) positive holes that can oxidize substrates [57]. The metal oxide is activated by exposure to UV light, visible light, or a combination of both. Consequently, photoexcited electrons are raised from the valence band to the conduction band, forming an electron–hole pair (e^-/h^+). This generated pair (e^-/h^+) has the capability to either reduce or oxidize a compound adsorbed on the photocatalyst's surface. These excitons initiate the oxidation or reduction of substrates and reactants on the surface of photocatalysts. The photocatalytic efficacy of the metal oxide originates from two distinct mechanisms: (i) the generation of $\bullet$OH radicals through the oxidation of OH^- anions and (ii) the production of O_2^- radicals through the reduction of O_2. Both these radicals and anions can subsequently interact with pollutants, resulting in their degradation or conversion into less harmful byproducts. These produced radicals and anions cause contaminants to degrade and change into byproducts with low risks [58]. In the following sections, the recent progress on the morphological dependence of TiO_2, ZnO, CuO, NiO, and WO_3 in the degradation of organic dyes in aqueous media will be presented.

4.1. Titanium Dioxide Photocatalysts

Since Fujishima and Honda's great discovery of water splitting in 1972 [59], great attention has been paid to utilizing the photocatalytic properties of some materials to convert solar energy into chemical energy for the oxidation or reduction of materials to produce useful materials such as hydrogen [60] and hydrocarbons [61], as well as to remove pollutants and bacteria from air, water, wall surfaces, and other environments [62,63].

TiO_2 has four polymorphs in nature, namely, tetragonal anatase, orthorhombic brookite, tetragonal rutile, and monoclinic. Two extra high-pressure forms were also produced using the rutile, TiO_2, and hollandite structures. Rutile, which is the most stable form of TiO_2, is the primary source of this compound. Conversely, anatase and brookite are metastable and transform into rutile during calcination [64]. TiO_2 is categorized as an n-type semiconductor and has varying energy bandgaps depending on its crystalline form. The energy bandgap is approximately 3.2 eV for anatase, 3.0 eV for rutile, and 3.2 eV for brookite [42]. Among the many different photocatalysts, TiO_2 has received the most attention and has been utilized in the most applications. This is due to its potent oxidizing properties [65–68], its ability to degrade organic pollutants [69], its superhydrophilicity [70], its chemical stability, long durability, nontoxicity, low cost, and transparency to visible light [62,71], as well as its good anti-corrosion performance, high mechanical strength, low density, and a competitive price.

TiO_2 exhibits photocatalytic properties by producing photogenerated charge carriers upon absorption of UV light which correspond to the energy band gap of TiO_2. These photogenerated holes in the valence band (VB) move to the TiO_2 surface and interact with adsorbed water molecules, resulting in the formation of hydroxyl radicals (●OH). Nearby organic molecules on the catalyst's surface are oxidized by the photogenerated holes and the ●OH radicals. Meanwhile, superoxide radical anions ($O_2^{\bullet-}$) are typically produced when molecular oxygen in the air reacts with electrons in reduction processes in the CB.

It has been reported that using pristine TiO_2 is not recommended because of its low electron transfer rate, light absorption, and electron–hole pair recombination. Thus, TiO_2 is produced in various nanostructures to improve electron transport and reduce electron–hole recombination in order to weaken these restrictions [72]. Several factors can significantly impact the effectiveness of photocatalytic systems, such as the size, specific surface area, pore volume, pore shape, crystalline phase, and exposed surface facets of the photocatalyst. Morphological factors can also affect photocatalytic performance as well as the properties of TiO_2 materials. Therefore, recently, there has been a lot of interest in the preparation of TiO_2 nano- or micro-structures with various morphologies [73,74], and a variety of TiO_2 nanostructural materials have been created, including spheres [74,75], nanorods [76], fibers [77], tubes [78], sheets [79], and interconnected architectures [80]. Due to their interconnected structure, three-dimensional (3D) monoliths may have high carrier mobility and be used in environmental decontamination as opposed to two-dimensional (2D) nanosheets, which have flat surfaces and good stickiness [69,81,82]. In the following section, the photocatalytic properties of TiO_2 with various morphologies are used for the breakdown of organic pigments.

In the last decade, Zhen et al. [83], simply treated amorphous anodic TiO_2 nanotubes (TiO_2 NTs) in situ hydrothermally at 70 °C to prepare anatase porous TiO_2 nanowires (TiO_2 NWs) (Figure 3a–f). The estimated BET surface area of the prepared TiO_2 NWs was 267.56 m^2 g^{-1}, nearly four times that of the utilized amorphous anodic TiO_2 NTs. The photocatalytic capability of porous TiO_2 NWs towards MB and Rhodamine 6G (Rh6G) were studied. Compared to TiO_2 NTs or Degussa P25, the porous TiO_2 NWs had superior photocatalytic activity (Figure 3g,h). The porous design and the substantial specific surface area are responsible for the increased photocatalytic activity.

Furthermore, anatase TiO_2 NWs were prepared by Lou et al. [84] using a facile one-pot solvothermal approach (Figure 4). Due to the high productivity and yield of the solvothermal reaction, a significant amount of what appears to be white mud is produced afterward. The choice of the DMF/HAc volumetric ratio in the solvent system used for synthesis determines whether the TiO_2 NWs assemble into hierarchical architectures or remain in freestanding form. The 1D nanostructure with outstanding photocatalytic activity for RhB degradation was perfectly preserved in both the synthesized and the annealed TiO_2 NWs.

Recent studies on the morphology of TiO_2 nanostructures in the photocatalytic degradation of several organic dyes (MB, MV, MO) have been published by Zhang et al. [85]. The balanced angle deposition technique (GLAD) was used to create nanorod, nanohelic, and nanozigzag TiO_2 nanofilms (Figure 5a). It can be observed that the morphology displayed significantly influences the performance of the photocatalytic degradation under UV–Vis light irradiation (Figure 5b,c). This is mostly explained by the variation in the produced nanostructures' specific surface area and pore volume. TiO_2 nanozigzag films demonstrate superior degradation capabilities compared to nanohelics and nanorods due to their extensive surface area, increased porosity, distribution of active sites at varying pore lengths, and the existence of oxygen vacancies.
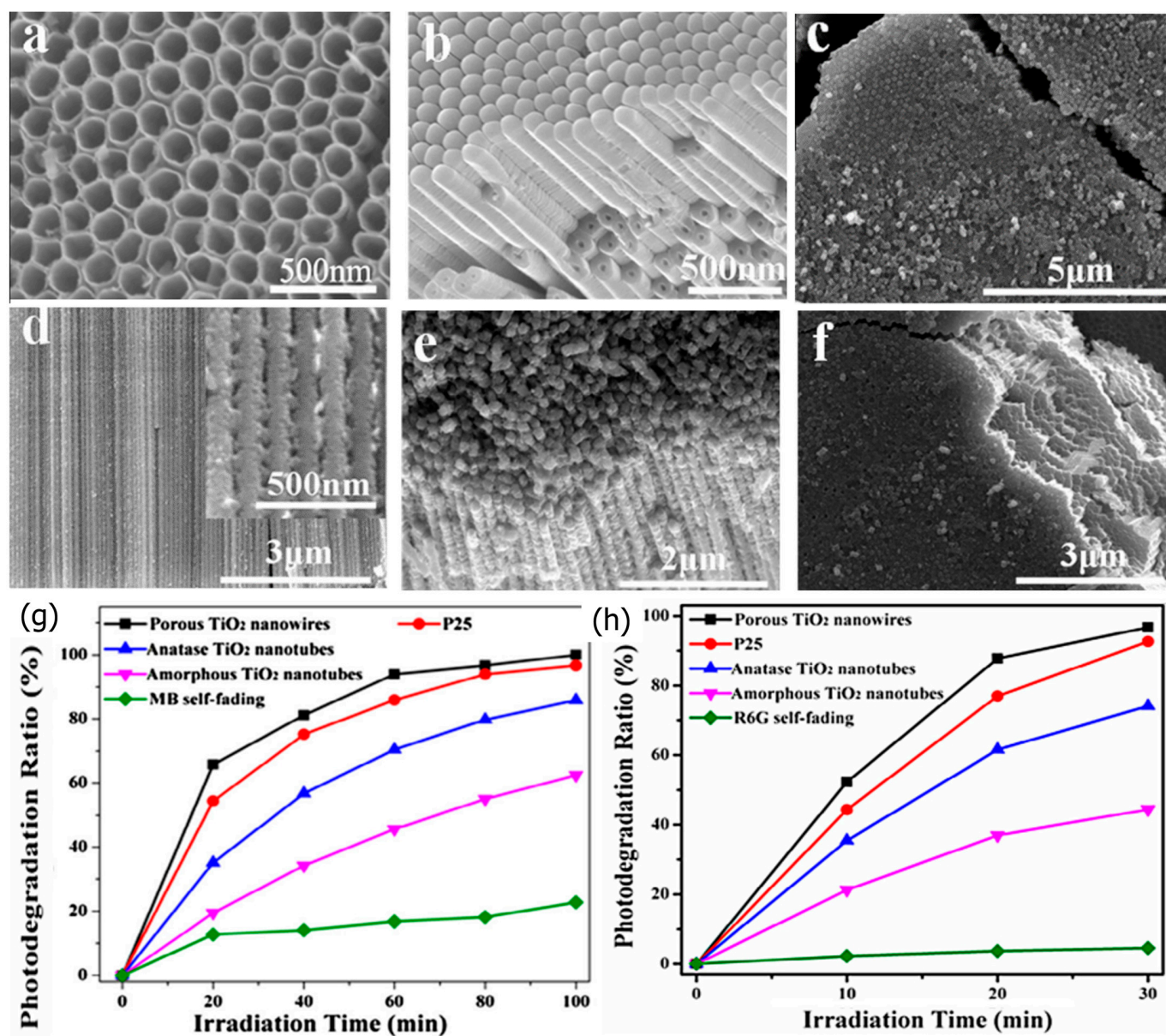
Figure 3. (**a**) SEM image of the anodic TiO$_2$ NTs, (**b**) cross-section and surface view image of the bottom side of the anodic TiO$_2$ NTs, (**c**) the porous TiO$_2$ NWs, (**d**) cross-section image of the porous TiO$_2$ NWs, (**e**) high and (**f**) low magnification cross-sections and surface views of the porous TiO$_2$ NWs. The photocatalytic degradation performance of (**g**) MB and (**h**) R6G with time of irradiation. Adopted with permission from Ref. [83] Copyright 2013, Elsevier.

By carefully hydrolyzing titanium tetrachloride (TiCl$_4$) with a homemade glass apparatus, Zidki et al. [86] prepared TiO$_2$ nanoparticles. The photoactive anatase and brookite phases make up the TiO$_2$ nanoparticles, as indicated by XRD and TEM/HRTEM image studies (Figure 6a,b). The photodegradation of MB and CR under UV–Vis light was used to illustrate the photocatalytic activity of TiO$_2$ nanoparticles. The degradation of MB showed that, in contrast to the CR degradation, the photocatalytic degradation of MB on TiO$_2$ nanoparticles is more effective in an alkaline environment (Figure 6c,d).
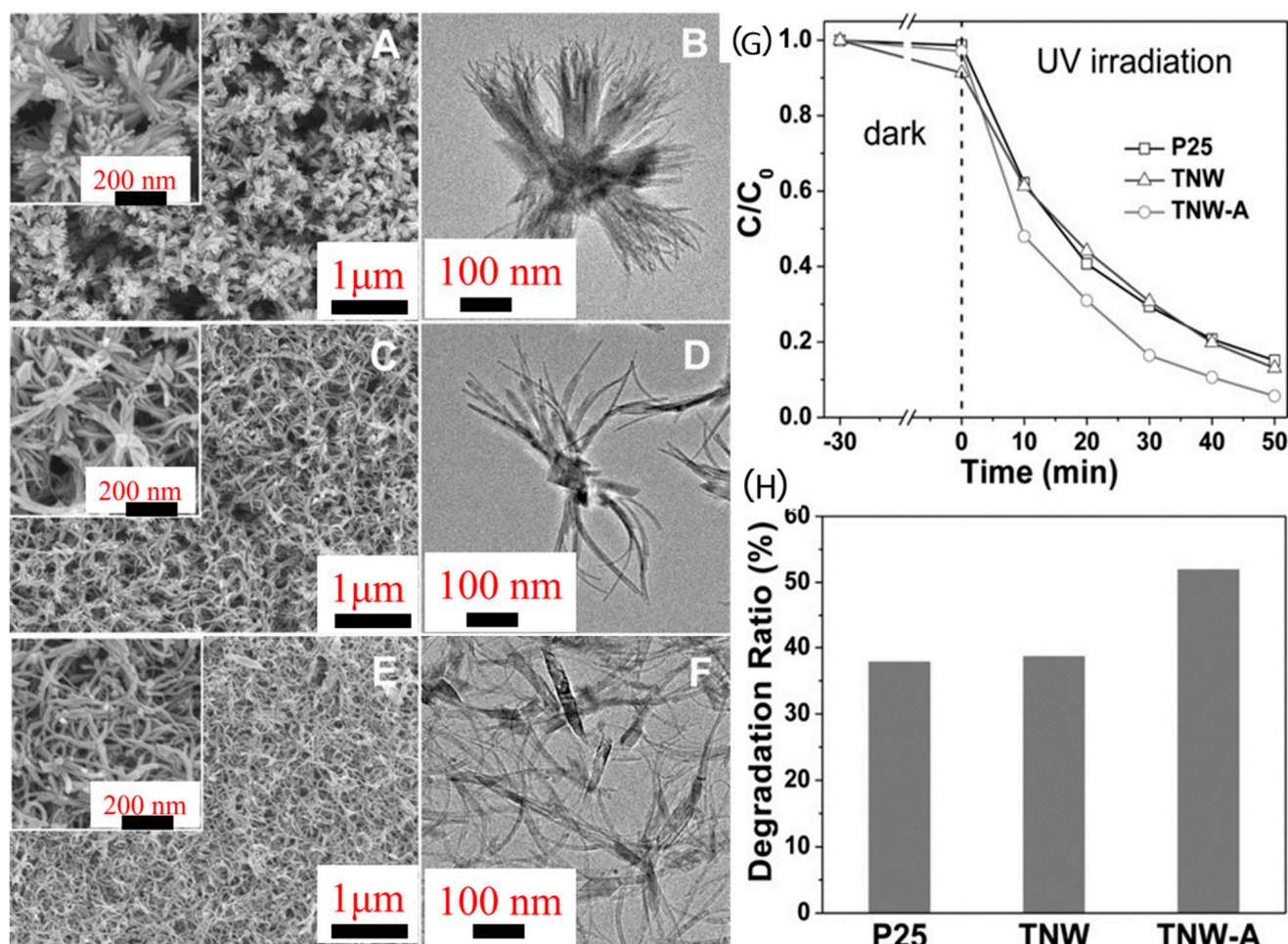
Figure 4. Morphological analysis (SEM and TEM images) of TiO$_2$ NWs prepared with different volumetric ratios of DMF/HAc: (**A**,**B**) 4/6, (**C**,**D**) 5/5, and (**E**,**F**) 6/4. (**G**) Photocatalytic degradation of RhB and (**H**) degradation ratio after 10 min irradiation over TNW, TNW $-$ A, and P25. Adopted with permission from Ref. [84] Copyright 2012, Wiley.

Habibi and Jamshidi [87] conducted a study in which they synthesized TiO$_2$ in various shapes using cellulose nanofibers (CNFs) as a template and a sol-gel technique. Three different forms of TiO$_2$ were produced: hydrogel, aerogel, and alcogel (as shown in Figure 7). The hydrogel-produced TiO$_2$ nanofibers were porous and strongly entangled, while the aerogel-produced TiO$_2$ had a sheet-like structure. The alcogel-produced TiO$_2$ had a structure similar to a hydrogel, but water was replaced with isopropanol. By using the Stober method with ammonia, the sol-gel process was modified by the researchers to produce TiO$_2$ nanowhiskers and nanosheets. The morphology of the nanowhiskers transformed into nanosheets as the ammonia level was raised, as confirmed by FESEM images. Moreover, the specific surface area of the TiO$_2$ samples was found to have increased. The photocatalytic efficiency of the prepared samples was examined using methylene blue (MB) as a model pollutant. All samples exhibited high photocatalytic efficiency under UV light, with over 98% degradation of MB in 2 h. Additionally, TiO$_2$ nanowhiskers displayed higher photodegradation efficiency under visible light compared to TiO$_2$ NPs and nanosheets.
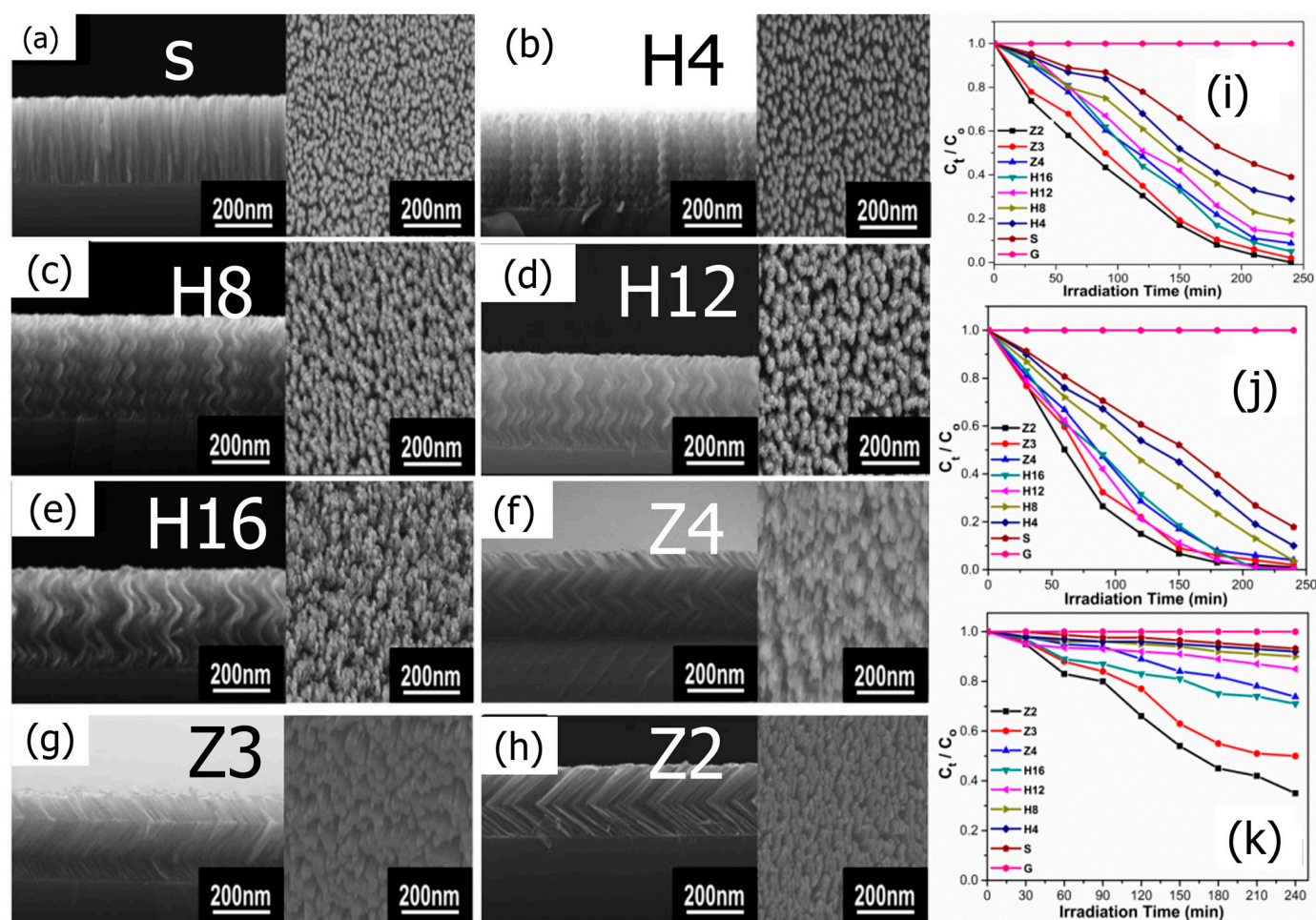
Figure 5. (**a**) SEM images (cross-sectional and top view) of TiO$_2$ nanostructures (**a**) Standing nanorod (**b**) Nanohelix-H4, (**c**) Nanohelix-H8, (**d**) Nanohelix-H12, (**e**) Nanohelix-H16, (**f**) Zigzag-Z4, (**g**) Zigzag-Z3, and (**h**) Zigzag-Z2. Pseudo-first-order kinetics (after exposure to UV–Vis light for 240 min for decolorization) of (**i**) MB, (**j**) MV, and (**k**) MO. Adopted with permission from Ref. [85] Copyright 2017, Elsevier.

TiO$_2$ NTs have received a lot of interest in recent years because of their one-dimensional ion exchange direction, increased surface area, and light absorption [88]. TiO$_2$ NTs can typically be made using one of three methods: hydrothermal, template, or electrochemical anodization. The most effective of these techniques, electrochemical anodization, is the least expensive and produces remarkably ordered nanotubes [89]. Additionally, the anodization technique stands out for its ability to control the morphology of nanotubes by simply changing the process parameters. In contrast to nanotubes grown over foils, Subramanian et al. [90] found that anodized TiO$_2$ NTs over titanium wires (TWs) significantly improved the photocatalytic degradation of MO.

In the presence of nanotubes grown on titanium wires, photocatalytic degradation rises from 20% to about 40%. Additionally, MO degradation in the presence of Pt-loaded TiO$_2$ nanotubes over foils matches the degradation in the presence of TiO$_2$ nanotubes on wires. This increased photoactivity is attributed to nanotubes formed in a radially outward orientation along a titanium backbone, which effectively absorb light that is reflected and refracted. Further enhancement was achieved by Rojviroon et al. [78]. In this study, electrochemical anodization was used to create TiO$_2$ nanotubes using thin titanium sheets at voltages of 20, 30, 40, and 50 V. The obtained TiO$_2$ nanotubes are shown in Figure 8a. The characterization investigation revealed that the inner diameter and depth of TiO$_2$ NTs

rose with increasing anodization voltages, but their wall thickness dropped. It seems that the TiO$_2$ NTs anodized at 50 V have shown promising photocatalytic activities towards the decolorization of indigo carmine (IC) and reactive black 5 (RB5) dyes. The decolorization efficiencies were measured to be 74.14% and 65.71%, respectively, under UV irradiation for 180 min and with an initial dye concentration of 4 μM. These results suggest that TiO$_2$ NTs anodized at 50 V can be a potential photocatalytic material for dye wastewater treatment.
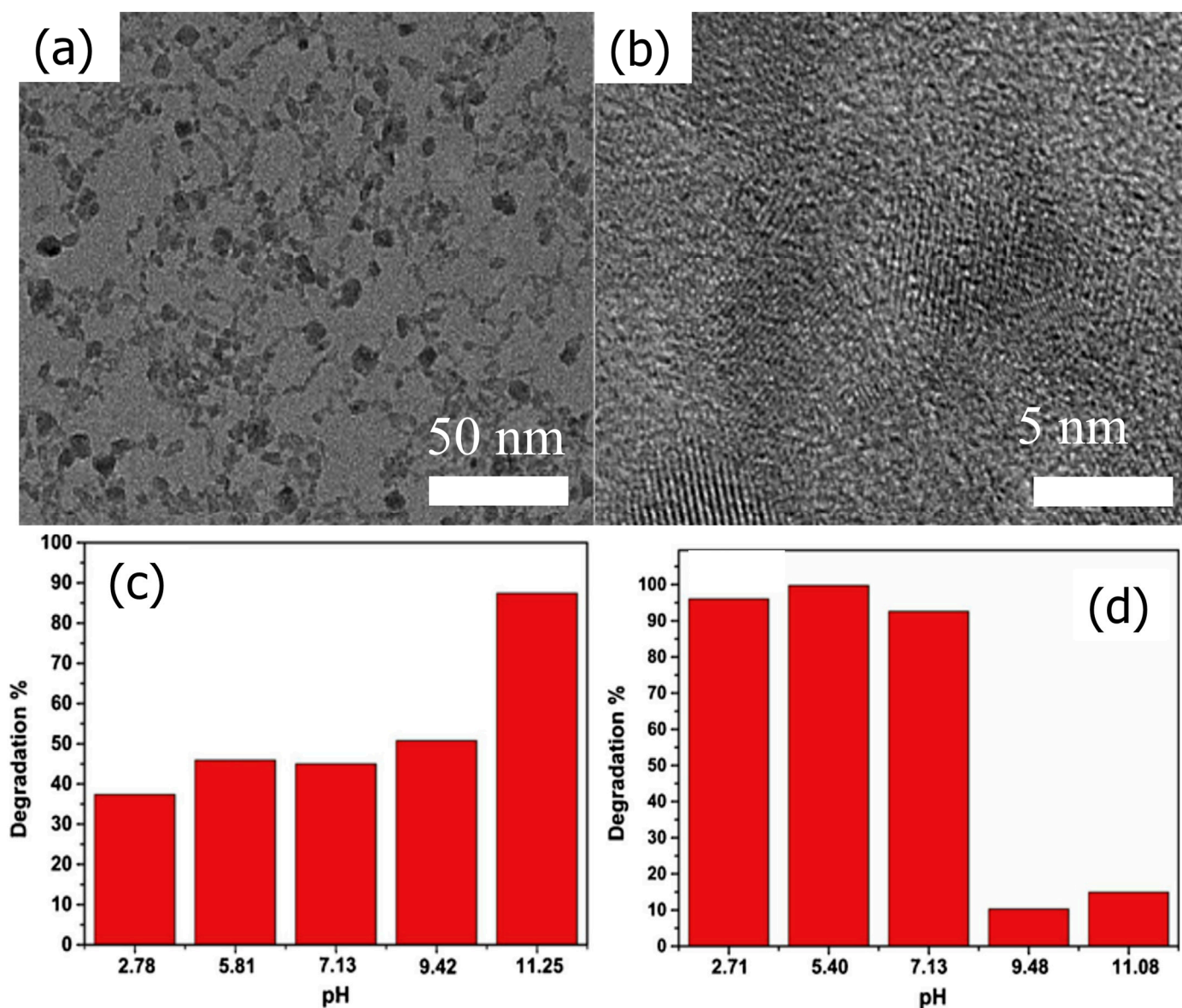
Figure 6. (**a**) TEM and (**b**) HR-TEM images of the prepared TiO$_2$ nanoparticles. Effect of pH on photodegradation of (**c**) MB and (**d**) CR dyes after under UV–Vis light illumination. Adopted with permission from Ref. [86] Copyright 2020, Elsevier.
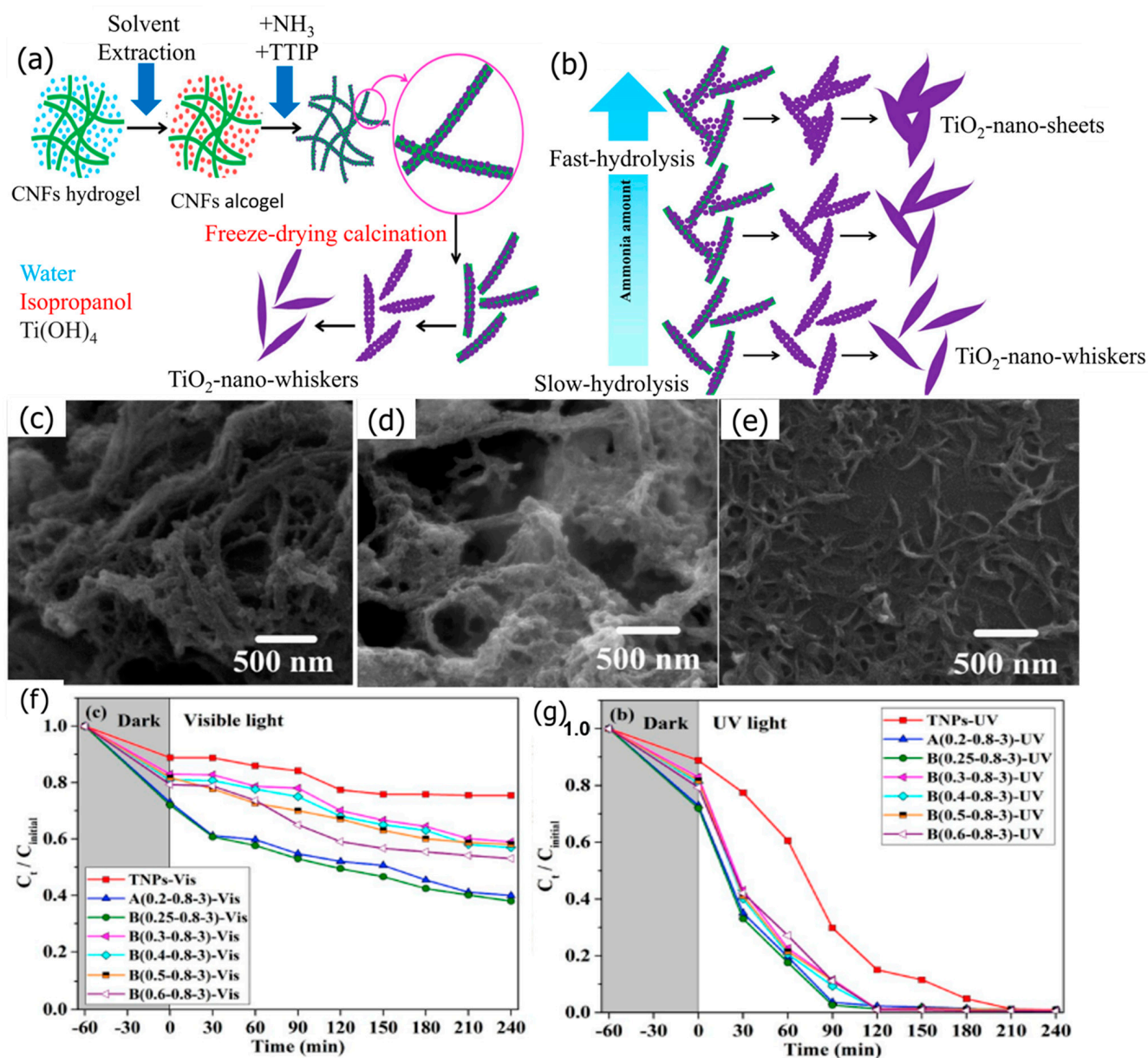
Figure 7. (**a**) Synthesis process of alcogel—TiO$_2$, (**b**) the shape evolution of alcogel—TiO$_2$ with an increasing ammonia amount. FESEM images of (**c**) hydrogel—TiO$_2$, (**d**) aerogel—TiO$_2$, (**e**) alcogel—TiO$_2$. Concentration changes in MB aqueous solution under (**f**) UV—and (**g**) visible light. Adopted with permission from Ref. [87] Copyright 2020, Elsevier.

Nozaki et al. [91] prepared TiO$_2$ nanosheet (TiO$_2$ NSs) photocatalysts for the degradation of MB when exposed to UV radiation (365 nm, 2.5 mW cm^{-2}). Ti(OBu)$_4$ and (NH$_4$)$_2$TiF$_6$ were both employed as starting materials, and a variety of samples with various side lengths were produced through hydrothermal synthesis by varying the F/Ti ratio between 0.3 and 2.0. Titania nanosheets produced with an F/Ti ratio of 0.3 led to the best degrading efficiency. The increase in surface area brought on by the reduction in size is what is responsible for the increased catalytic activity.
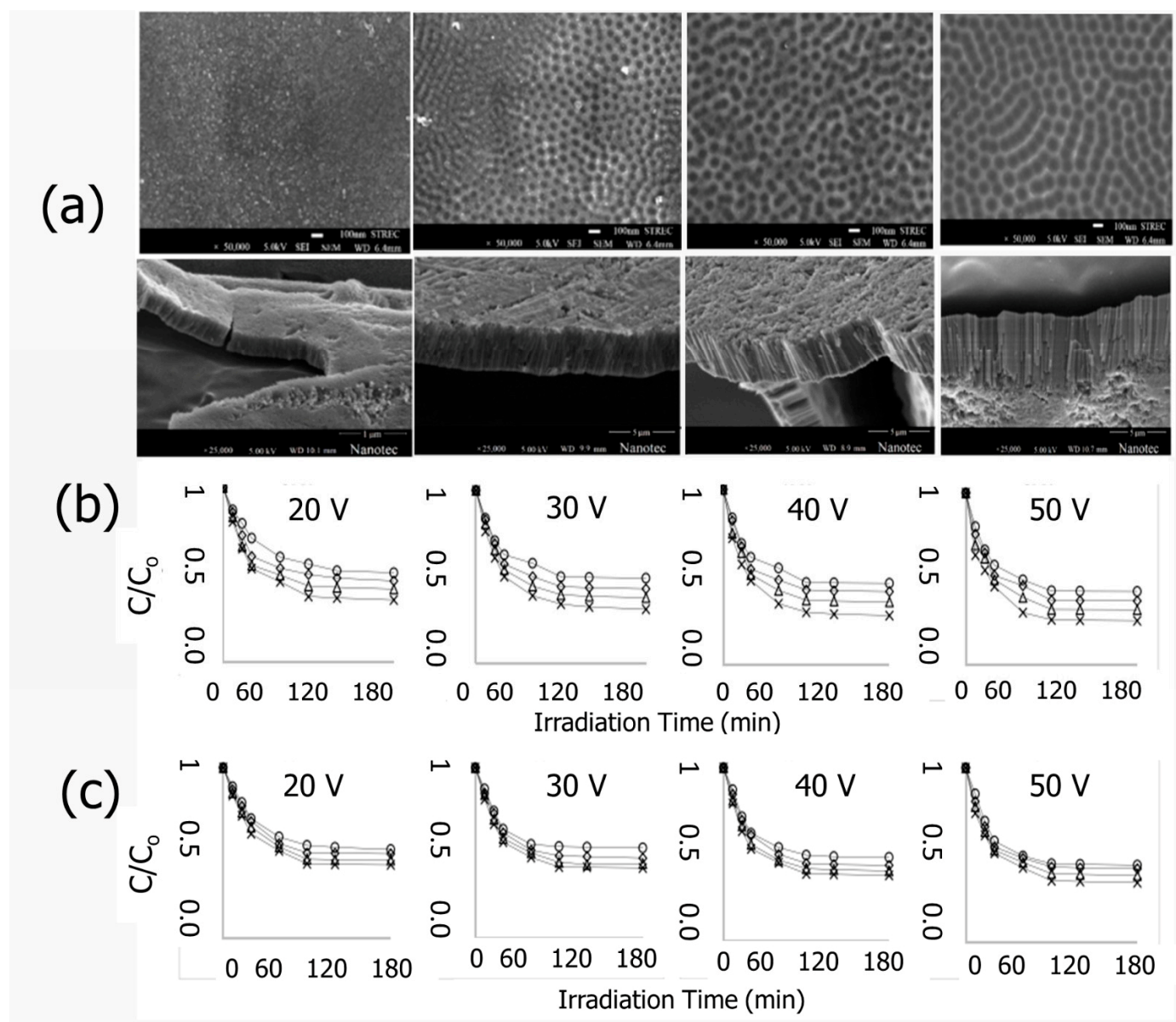
Figure 8. (**a**) FE-SEM images of TiO$_2$ NTs anodized at 20, 30, 40, and 50 V. Photocatalytic decolorization using TiO$_2$ NTs sheets anodized at 20–50 V for various initial concentrations of (**b**) IC and (**c**) RB5. Adopted with permission from Ref. [78] Copyright 2021, Elsevier.

Recently, Nair developed a floating photocatalyst to accelerate the photocatalytic degradation of a TiO$_2$ nanosheet in a cellulose acetate matrix and supplied support using ethylene vinyl acetate (Figure 9a–c) [92]. The degradation of CR dye by a floating photocatalyst made of TiO$_2$ nanosheets performed well in both UV and solar light (Figure 9d,e).
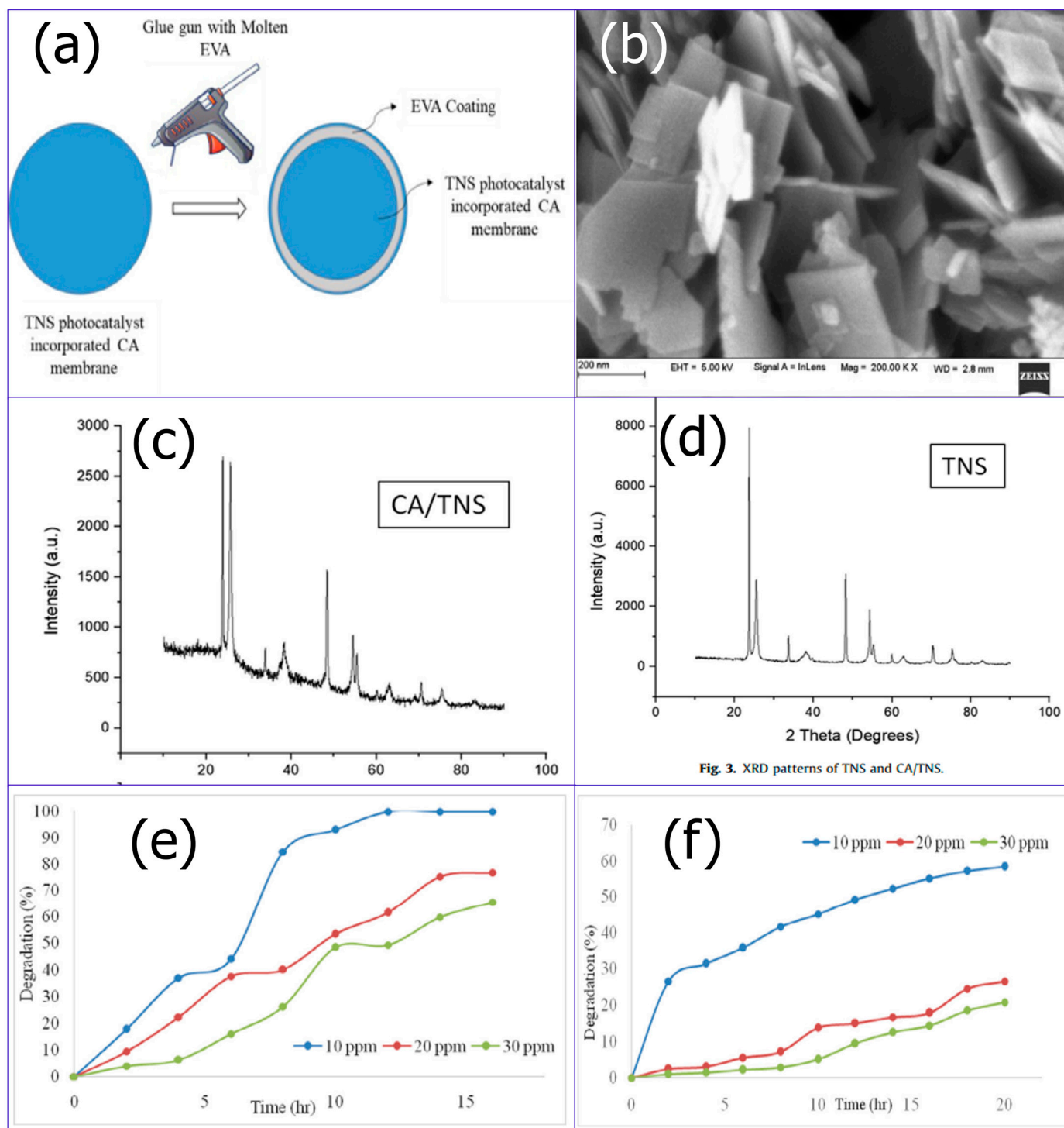
Figure 9. (**a**) Schematic representation of the synthesis of a floating photocatalyst, (**b**) FESEM image of TiO_2 NSs. XRD of TiO_2 NSs (**c**) and CA/TiO_2 NSs (**d**), (**e**) Solar degradation study of CR dye using a floating photocatalyst, and (**f**) UV degradation of CR dye using a floating photocatalyst. Adopted with permission from Ref. [92] Copyright 2021, Elsevier.
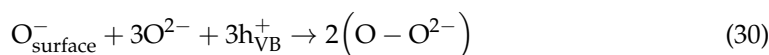
4.2. Zinc Oxide Photocatalysts

ZnO is commonly found in a hexagonal wurtzite crystal structure, which has a non-centrosymmetric lattice and exhibits piezoelectric and pyroelectric properties. The crystal structure also affects the photocatalytic activity of ZnO, with the (001) crystal facet showing

the highest photocatalytic activity due to its high surface energy and abundance of surface defects [93,94]. The photocatalytic activity of ZnO is attributed to the formation of electron–hole pairs upon the absorption of light with energy equal to or greater than its bandgap energy. The photogenerated holes can oxidize water or hydroxide ions to produce hydroxyl radicals, while the photogenerated electrons can reduce oxygen or organic molecules [95]. However, the recombination of electron–hole pairs limits the efficiency of photocatalytic reactions, and various strategies have been employed to enhance the separation of photo-generated charge carriers and improve the photocatalytic activity of ZnO, including doping with transition metals, surface modification with noble metals or semiconductors, and use of a heterostructure with other semiconductors [95,96].

Until now, various morphologies of ZnO nanomaterials such as nanorods, nanowires, nanotubes, and hollow structures have been prepared [97]. ZnO nanomaterials are usually prepared via different techniques including evaporative decomposition of solution [98], solid state reaction [99], sol-gel [100], and so on. The preparation technique shows a noticeable effect on the particle size and the morphology, which directly affects the physical and chemical properties of the prepared ZnO nanostructured materials. As reported by Singh et al., the morphology of ZnO nanostructures can be controlled by adding additives or capping agents such as triethanolamine (TEA), oleic acid, and thioglycerol [101]. The creation of ZnO nanostructures with different morphologies requires the application of many surfactants, including sodium dodecyl sulfate (SDS), tetraethylammonium bromide (TEAB), and cetyltrimethylammonium bromide (CTAB). The photocatalytic activity of ZnO is significantly influenced by its structural morphology [102,103]. This influence stems from the crystal structure, which facilitates the separation of charge carriers. However, some studies have shown that non-spherical morphologies such as nanorods and nanowires can also exhibit enhanced photocatalytic performance due to their unique crystal facets and surface areas, which can promote charge transfer and improve catalytic efficiency. Ultimately, the selection of a particular morphology for a photocatalyst relies on the specific application and the desired properties. The flake-like structure, however, exhibits comparatively lower performance [102].

Although a great deal of attention has been devoted to the photocatalytic activity of ZnO, its photocatalytic activity suffers from the following drawbacks: (i) the large bandgap of ZnO (3.37 eV), which inhibits light absorption in the UV (380 nm) range, which means ZnO cannot absorb visible light, drastically lowering photocatalytic efficiency [104,105]; (ii) the degradation reactions at the semiconductor–liquid interface are slowed down by the quick recombination of the charge carriers; (iii) the difficulties of using a traditional filtration process to recover ZnO powder from a suspension; (iv) the propensity to clump together during catalytic processes and the vulnerability to UV-induced corrosion; and (v) photocorrosion is one of the main restrictions of ZnO as a photocatalyst for wastewater treatment [106]. The following four phases describe how photocorrosion occurs [107].

$$O_{surface}^{2-} + h_{VB}^{+} \rightarrow O_{surface}^{-} \tag{29}$$

$$O_{surface}^{-} + 3O^{2-} + 3h_{VB}^{+} \rightarrow 2\left(O - O^{2-}\right) \tag{30}$$

$$\left(O - O^{2-}\right) + 2h_{VB}^{+} \rightarrow O_2 \tag{31}$$

$$2Zn^{2+} \rightarrow 2Zn^{2+}aq \tag{32}$$

The net equation for the photocorrosion of ZnO is shown below.

$$ZnO + 2h_{VB}^{+} \rightarrow Zn^{2+} + \frac{1}{2}O_2 \tag{33}$$
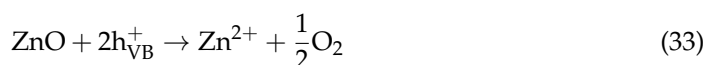
Therefore, the majority of ZnO photocatalytic studies have been carried out under UV radiation. Recently, various studies have been conducted on utilizing ZnO with different morphologies for the elimination of organic pollutants. To use as a photodegradation for

MO dye, Bhatia and Verma [108] synthesized ZnO nanoparticles (ZnO NPs) with varying defect concentrations by burning at 700 °C and subsequent quenching in air.

From FESEM images (Figure 10a–d), ZnO NPs are less than 45 nm in size, and an uneven grain boundary distribution was discovered in the quenching-induced defects. The improvement of the photocatalytic effectiveness of synthesized nanoparticles is greatly influenced by their various morphologies. The photodegradation of MO dye has been proven to follow a first order model through kinetic analysis, with a rate constant of 0.0165 min^{-1}. (Figure 10f). Additionally,, it has been reported that approximately 100% MO degradation has been achieved in 150 min under UV irradiation (Figure 10e). Recently Dodoo-Arhin prepared ZnO NPs using the sol-gel method, with zinc acetate as a Zn source [109]. The effect of calcination temperature on the particle size of ZnO was investigated. As shown in SEM, the obtained wurtzite ZnO NPs showed crystallite sizes ranging from 16 nm to 30 nm. Increasing the calcination temperature increases the crystallite size and reduces the energy band gap of the obtained ZnO NPs. In addition, the prepared ZnO showed a rice-like microstructure morphology (Figure 10g–i). The prepared ZnO NPs were utilized as a photocatalyst toward the degradation of RhB dye under UV– light. The obtained analysis showed that ZnO NPs calcined at 400 °C obtained the highest degradation efficiency (95.41%), as shown in Figure 10h.

ZnO NPs also showed important catalytic activity under solar illumination. For example, ZnO NPs of various morphologies were developed by Saikia et al. [110] for the photodegradation of malachite green (MG) (Figure 11a–d). Under solar light, the flower-shaped homocentric bundles of hydrothermally synthesized ZnO nanorods (ZnO NRs) in the form of pencil-like structures demonstrate outstanding photocatalytic activity, as evidenced by the pseudo first-order kinetics of the Langmuir–Hinshelwood model in the photodegradation of MG dye (Figure 11e,f). Additionally, ZnO NPs and homocentric pencil-like ZNRs bundles in the shape of flowers were prepared.

Additionally, photocatalytic degradation of organic dyes by ZnO nanosheets (ZnO NSs) was also investigated. For example, Komarneni et al. [111] used a simple, ultra-rapid solution approach to create ZnO NSs with many oxygen-vacancy defects. The surface area was significantly increased from 6.7 to 34.5 m^2 g^{-1} by the addition of 1 mol L^{-1} Na$_2$SO$_4$. With a rate constant of 0.0179 min^{-1} under visible light (>420 nm), the as-prepared ZnO NSs showed abundant oxygen vacancies, which are crucial for improving visible light absorption and, consequently, high photocatalytic activities towards the degradation of RhB. These rates were about 13 and 11 times higher, respectively, than those of ZnO NPs with few oxygen defects.

Further enhancement with a rate constant k = 0.0421 min^{-1} was achieved by hybridized ZnO NSs with Ag$_3$PO$_4$ nanoparticles. A synergistic effect of surface oxygen vacancies and Ag$_3$PO$_4$ coupling was suggested by this augmentation, which was attributed to the improved visible light absorption as well as the well-matched energy level that is responsible for effective charge transfer between oxygen-vacancy-rich ZnO NSs and Ag$_3$PO$_4$. ZnO nanowires also display a significant superior photocatalytic activity toward organic dye degradation. For example, by using a low-cost, low-temperature hydrothermal approach, Leprince-Wang et al. [112] demonstrated an effective synthesis of nontoxic, biocompatible ZnO nanostructures only on the surface of commercially available concrete and tiling pavements (Figure 12a–e).

The obtained data showed an enhancement in photocatalytic activity for degrading organic dyes in aqueous media with high photocatalytic stability (Figure 12f–h).

The degradation of Acid Red 57 (AR57) under UV irradiation was studied further by El-Bindary et al. [113]. In this study, ZnO nanowires (ZnO NWs) were prepared by a low-temperature co-precipitation technique employing zinc sulfate as a precursor. After 190 min, the effectiveness of the photocatalytic degradation of ZnO NWs produced at 400, 500, and 600 °C was 90.03, 77.67, and 72.71%, respectively. Moreover, the degradation of AR57 fitted first-order kinetics. Recently, the effect of several kinds of organic dyes as a guiding agent for the formation of ZnO NWs was described by Yang et al. [114].
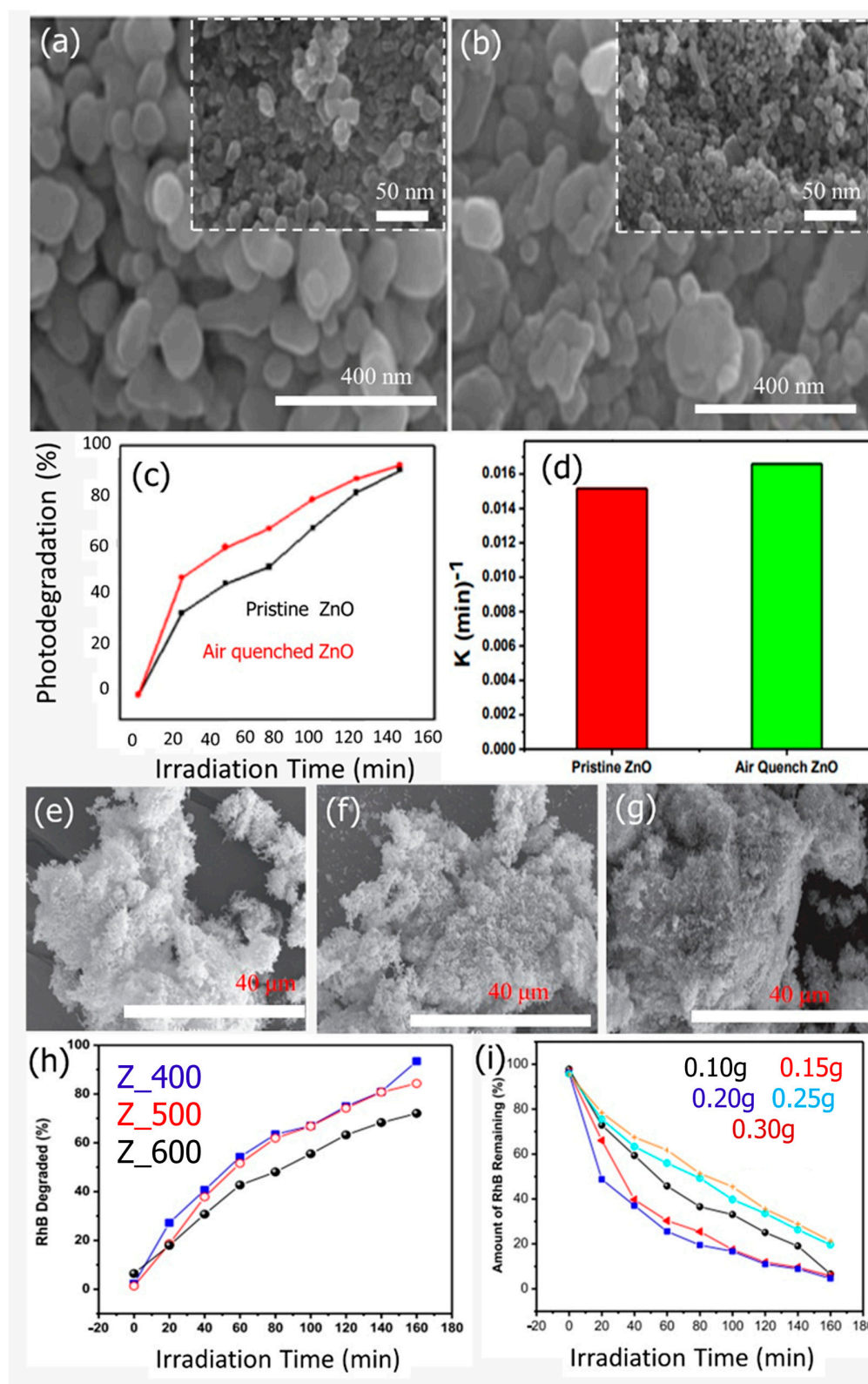
Figure 10. (**a**) Low and high magnification SEM images of ZnO, (**b**) air quenched ZnO, (**c**) photodegradation vs. irradiation time of MO dye for pristine ZnO and air quenched ZnO, (**d**) rate constant for after 150 min of UV exposure (Adopted with permission from Ref. [108] Copyright 2017, Elsevier), SEM images of ZnO calcined at (**e**) 400 °C, (**f**) 500 °C, and (**g**) 600 °C. (**h**) RhB degradation vs. irradiation time and (**i**) the effect of the catalyst load on RhB degradation (Adopted with permission from Ref. [109] Copyright 2019, Elsevier).
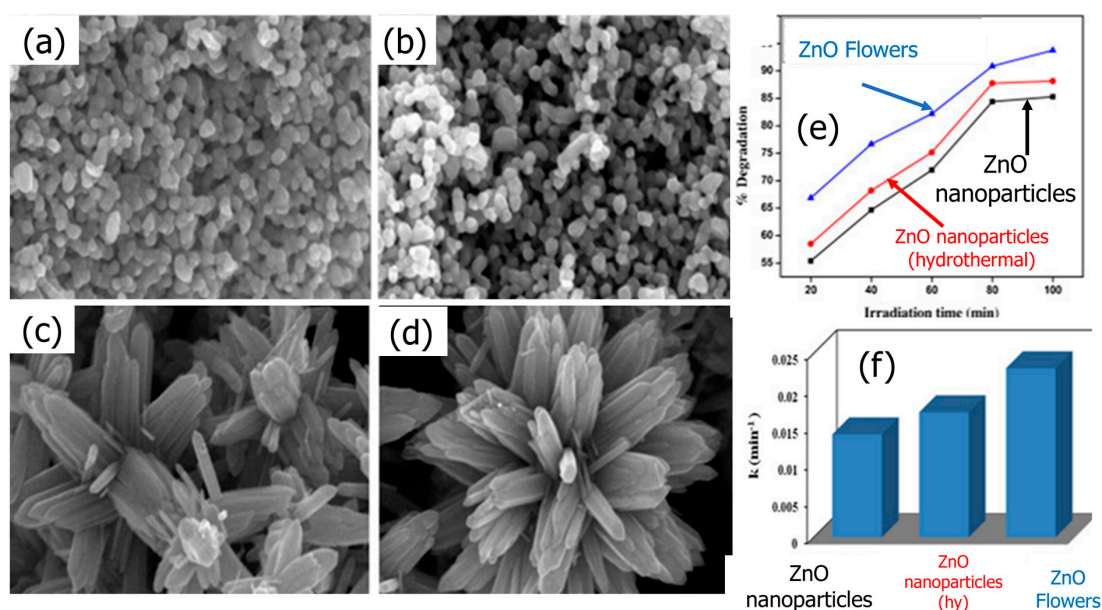
Figure 11. FE-SEM images of (**a**) ZnO NPs, (**b**) ZnO NPs (hydrothermal), (**c**) ZnO flowers, (**d**) one ZnO flower, (**e**) comparative photodegradation of MG by ZnO NPs, and (**f**) the estimated rate constant for photodegradation of MG by ZnO NPs under solar light. Adopted with permission from Ref. [103] Copyright 2014, Elsevier.
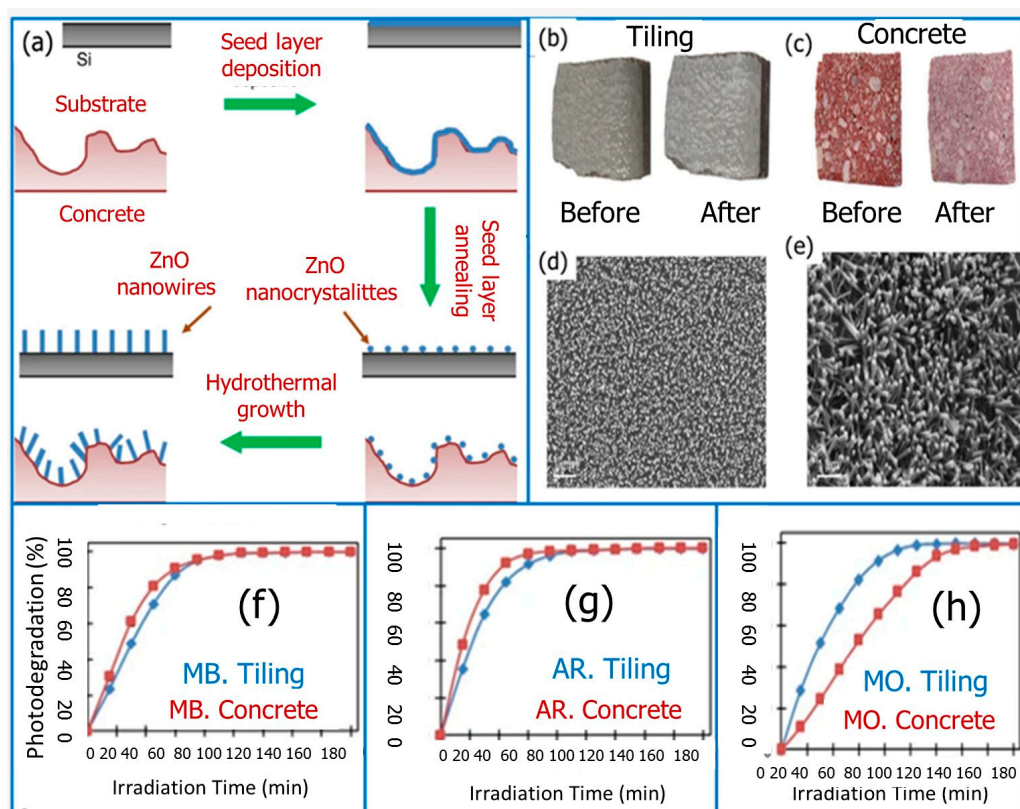
Figure 12. (**a**) Scheme of the ZnO NWs growth on a flat substrate (i.e., Si wafer) vs. a construction material (i.e., concrete), (**b**) top views of the gray tiling, and (**c**) red concrete pavement before and after the growth of ZnO nanostructures. (**d**) SEM top-view of ZnO NWs on the tiling surface, (**e**) ZnO NRs on the concrete surface, and (**f**–**h**) the photodegradation rate of MB, AR, and MO dyes vs. time. Adopted with permission from Ref. [112] Copyright 2019, Springer Nature.

EBT was found to effectively direct the growth of ZnO NWs, inhibiting their growth along the c-axis direction. Additionally, the introduction of UV light during growth significantly enhanced the photocatalytic degradation of EBT absorbed on the surface of the ZnO NWs. ZnO NWs arrays grown on glass fiber cloth with a dominant exposed polar (0001) facet exhibited superior photocatalytic performance compared to other arrays.

4.3. Copper Oxide Photocatalysts

Copper (II) oxide, also known as cupric oxide (CuO), is a naturally occurring p-type semiconducting metal oxide. This is due to the presence of oxygen vacancy defects in its crystal structure. CuO has an indirect small bandgap of 1.2 eV at room temperature [115]. Copper also exists in other polymorphs such as copper (I) oxide, commonly known as cuprous oxide (Cu_2O), and copper (III) oxide (Cu_4O_3). CuO displays higher thermal stability than Cu_2O, whereas Cu_4O_3 is a challenging metastable phase due to its mixed copper atom oxidation state, making its synthesis problematic [116,117]. CuO is a brownish-black powder that is used in various applications, such as catalysis, chemical and gas sensors, superconductors, and energy conversion and storage devices, as well as in biomedicine and textile production [118–120]. CuO has been extensively used as a heterogeneous catalyst in diverse chemical processes such as the oxidation of carbon monoxide (CO), hydrocarbons, and phenol in supercritical water, the selective catalytic reduction of nitric oxide with ammonia, and the breakdown of nitrous oxide [121].

Furthermore, CuO has been investigated as a photocatalytic material [122]. Additionally, it has been reported how the bandgap of CuO nanostructures is influenced by their morphology [123]. The subsequent section will demonstrate the effectiveness of CuO nanostructures as a photocatalyst for eliminating organic dyes from aqueous solutions, including an analysis of the removal mechanism and the impact of morphology on the removal efficiency.

CuO nanostructures are among the interesting photocatalytic materials usually utilized for the removal of various organic pollutants due to their high abundance, low cost, narrower bandgap, excellent chemical stability, and facile synthesis [124]. The narrow bandgap of CuO makes it active in the visible region of the electromagnetic spectrum. To enhance the catalytic activity of CuO, H_2O_2 is often added to the reaction mixture. H_2O_2 is a better electron acceptor than O_2, so it quickly captures the photogenerated electrons from the photocatalyst's surface, becoming reduced and forming hydroxyl radicals ($^\bullet OH$) [125]. This is important for offering more active radicals, as well as reducing the rate of electron–hole recombination, which boosts the utilization of holes during the photocatalytic process. Without H_2O_2, CuO displays an inability to generate a sufficient amount of $^\bullet OH$ radicals, and thus CuO is considered as an ineffective photocatalyst for degrading organic pollutants [126]. This is because the redox potential required to produce $^\bullet OH$ radicals is higher than the VBs of CuO. Thus, CuO has weaker oxidative capabilities for the breakdown of organic contaminants and cannot produce hydroxyl radicals when illuminated. There are many works that indicate that without H_2O_2, CuO in different morphologies displays no catalytic activity, as reported by He et al. [127]. Recently Latief et al. prepared CuO NPs with a range of sizes between 25 and 90 nm (Figure 13a,b) to deprecate CR dye from aqueous solutions. The analysis showed that the addition of H_2O_2 to CuO NPs significantly enhanced the degradation of CR dye under UV light, as presented in Figure 13c. In addition, increases in H_2O_2 result in improvements in the degradation rate (Figure 13d).

CuO nanostructures with various morphologies, including flower-like, boat-like, plate-like, and ellipsoid-like structures, were prepared and showed excellent catalytic activity towards the degradation of MB. However, without H_2O_2, the degradation stopped after 15 h, highlighting the significant dependence of CuO nanostructure photocatalytic activity on H_2O_2. Adsorption–oxidation–desorption is the postulated possible mechanism for the photocatalytic degradation of dyes by CuO in the presence of H_2O_2 under light illumination [127]. In this mechanism, various free radicals such as $HO^\bullet$, $HOO^\bullet$, and O_2^- are

mainly responsible for the degradation of dyes. The first step is adsorption of dye and H_2O_2 molecules on the surface of the CuO nanostructure. The second step involves the decomposition of H_2O_2 into free radicals ($HO^{\cdot}$, $HOO^{\cdot}$, or O_2^{-}). These free radicals display a high oxidative ability to oxidize the organic dye. The third step involves desorption of the small molecules from the CuO surface, and finally the catalyst is recovered [128].
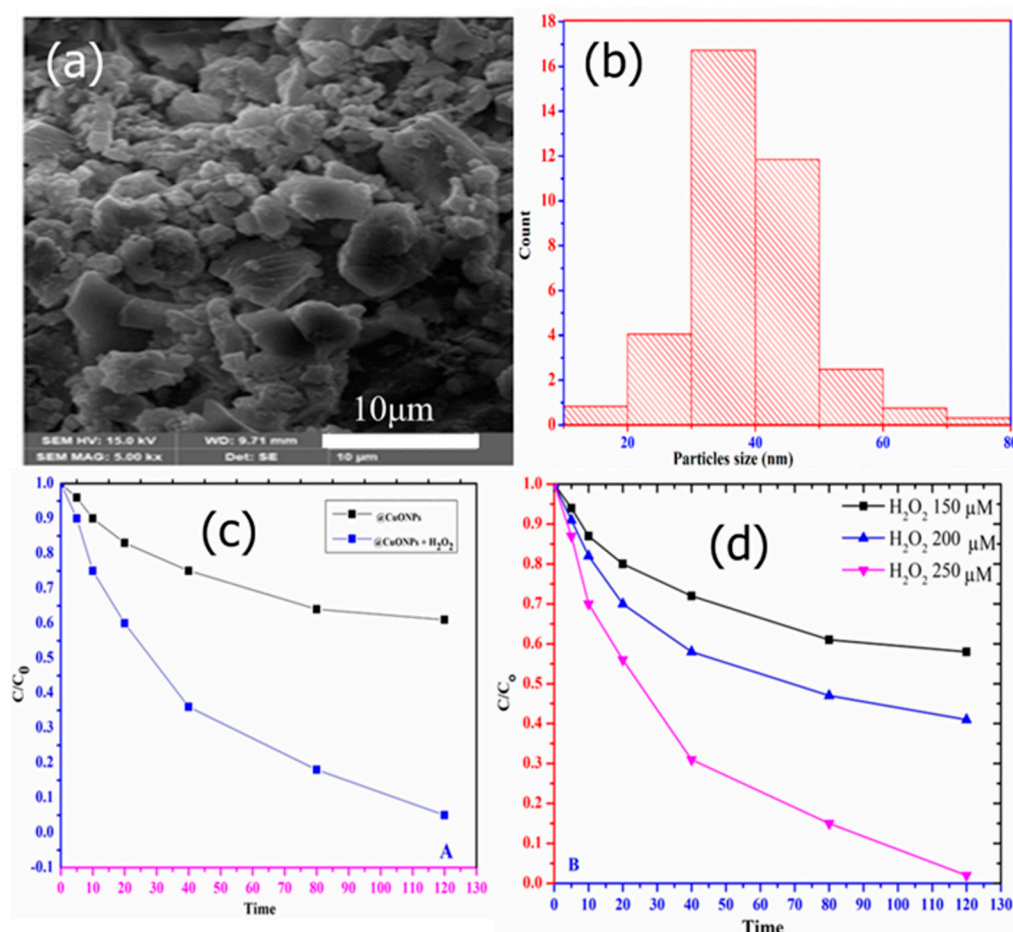

Figure 13. (**a**) SEM image of CuO NPs, (**b**) histogram spectrum of CuO NPs, (**c**) effect and removal of CR dye by UV/H_2O_2, and (**d**) effect of H_2O_2 concentration in the degradation of CR dyes (Adopted with permission from Ref. [125] Copyright 2023, MDPI).

Morphology is a critical factor that affects the photocatalytic activity of CuO nanostructures toward the degradation of organic dyes. For example, Wang et al. reported that CuO nanowires (Figure 14a,b) showed excellent catalytic activity toward the degradation of RhB [129]. The CuO nanowires demonstrated a total degradation efficiency of 95.5% after 9 h of UV light irradiation (as shown in Figure 14c), which was significantly higher than that of commercial CuO powders (which achieved only 39.6% degradation). In addition, Sadollahkhani et al. investigated the photocatalytic performance of CuO nanoparticles with various morphologies (as depicted in Figure 14d–f) for the degradation of CR dye under UV illumination [130]. The decomposition of CR dye takes place on the surface of CuO; thus, adsorption plays a critical role in the photocatalytic degradation. Samples doped with Zn appear to have improved degradation performance (63%) according to the photocatalytic examination of the degradation of MB dye (Figure 14g). The photocatalytic studies revealed that the degradation of CR for nanorods was the highest among the other prepared materials, with a total degradation efficiency of 67% after 210 min irradiation (Figure 14h). Moreover, the CR degradation reaction follows a first order kinetics model with the three CuO morphologies. On the other hand, Anandan et al. [131] prepared

dandelion-like CuO microspheres with sizes of ~1–2 μm through the ultrasound process without any surfactants. The photocatalytic performance of the CuO nanoparticles that were synthesized was investigated for the degradation of Reactive Black-5. The study found that the CuO microspheres with a dandelion-like morphology exhibited excellent photocatalytic activity, with approximately 76% of the dye degraded in just 5 h under visible light exposure. The degradation reaction followed a pseudo-first-order kinetic model, with a rate constant of 0.312 h^{-1}. Recently, George et al. prepared flowers similar to CuO 3D nanostructures doped with nickel, zinc, and iron (Figure 14h) [132].
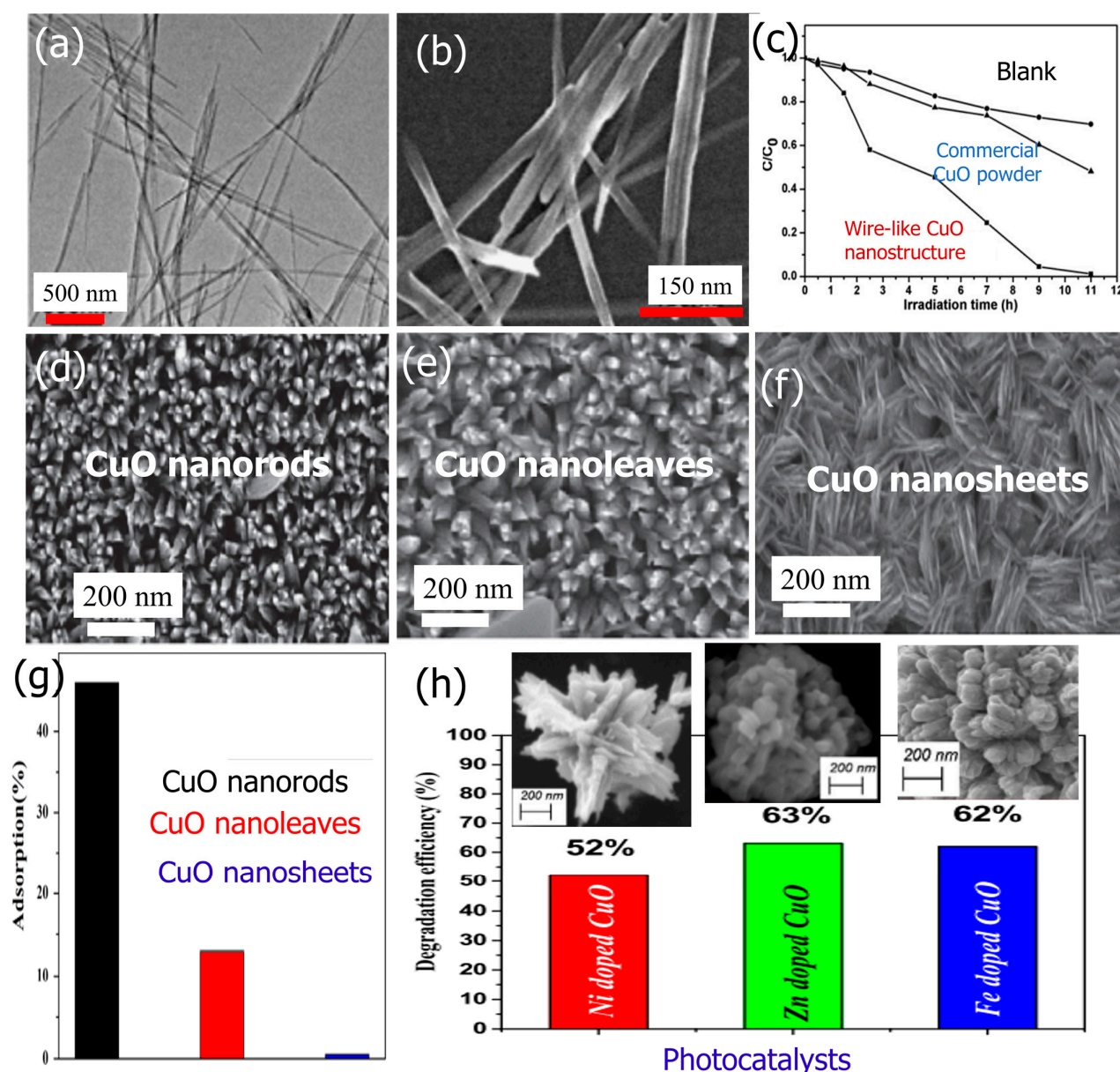
Figure 14. (**a**) TEM and (**b**) SEM images of CuO nanowires, (**c**) the photocatalytic efficiency of RhB degradation on different catalysts in the presence of CuO nanowire catalyst (Adopted with permission from Ref. [129] Copyright 2012, Elsevier), (**d**–**f**) SEM images of different CuO morphologies, (**g**) adsorption of CR on the surface of different morphologies of CuO [Initial CR concentration is 20 mg L^{-1}, dose of CuO is 0.05 g, and stirring time is 30 min] (Adopted with permission from Ref. [130] Copyright 2014, Elsevier), and (**h**) photocatalytic degradation efficiency of MB dye using Ni, Zn, and Fe-doped CuO (together with their SEM images) (Adopted with permission from Ref. [130] Copyright 2021, Elsevier).

Using NaBH$_4$ as q reducing agent in an aqueous medium, Nazim et al. [133] recently synthesized porous CuO nanosheets (Figure 15a) for use as a photocatalyst towards the degradation of food dye. The optical energy band gap of the prepared CuO was found to be approximately 1.92 eV. The CuO nanosheets were tested as photocatalysts for the degradation of Allura Red AC (AR) dye and showed excellent photocatalytic degradation efficiency of around 96.99% in just 6 min under visible light irradiation at room temperature (Figure 15b,c). The photodegradation kinetics of AR followed a pseudo-first-order reaction model, with a rate constant of 0.524 min^{-1}. Additionally, the CuO nanosheets exhibited remarkable recycling ability for AR degradation (Figure 15d).
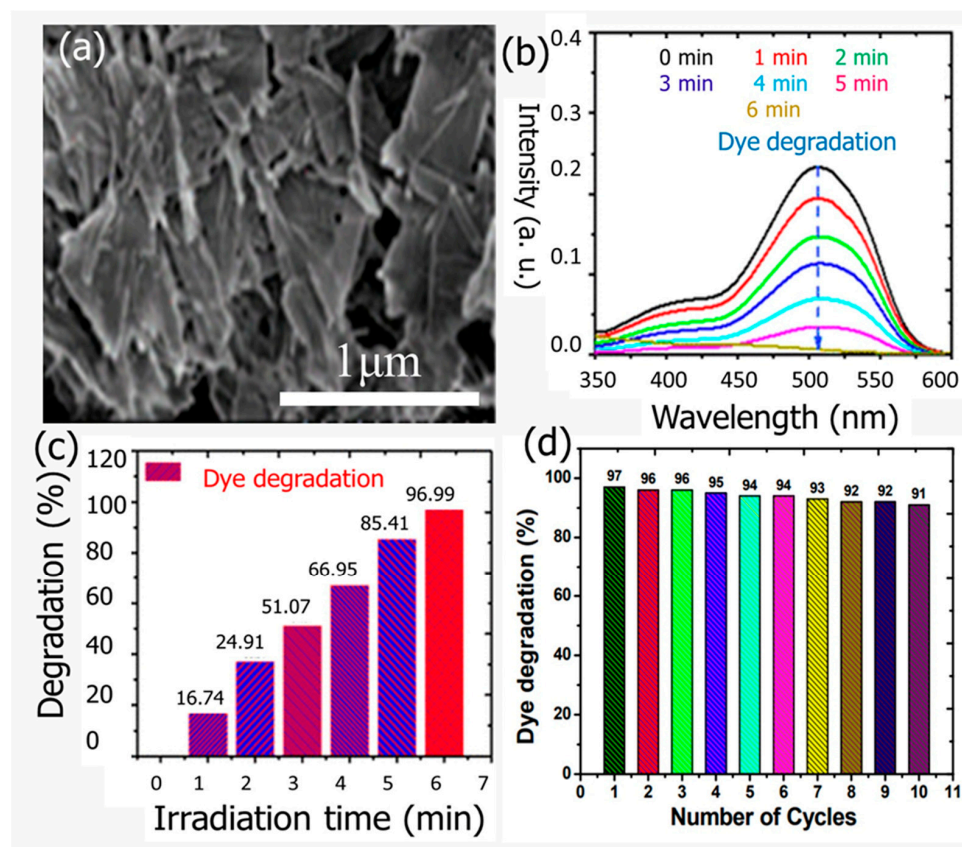
Figure 15. (**a**) FESEM images of CuO nanosheets, (**b**) UV–Vis spectrum of dye degradation at different times, (**c**) gradual degradation histogram against time of the AR dye in aqueous medium, and (**d**) recyclability of the CuO nanosheets after ten degradation cycles for AR dye. Adopted with permission from Ref. [133] Copyright 2021, American Chemical Society.

4.4. Nickle Oxide Photocatalysts

NiO is a broad bandgap (3.6–4.0 eV) p-type semiconducting oxide. NiO has attracted a lot of attention due to its application in numerous areas, including fuel cell electrodes, battery cathodes, dye-sensitized solar cells, etc. [134–137].

In addition, NiO displays a promising ability to produce OH radicals and thus is a potential candidate toward the degradation of organic pollutants. For example, Jayakumar et al. [138] prepared NiO nanoparticles through a chemical precipitation method for use as photocatalysts for the degradation of MB dye in aqueous media. The photocatalytic degradation results showed that the NiO nanoparticles are potential photocatalysts for the degradation of MB dye.

Saeed et al. utilized a chemical reduction process to prepare NiO NPs and NiO/nanoclay nanocomposite (NiO/Nc) and evaluated their photocatalytic efficiency for the degradation of orange II dyes in aqueous solution [139]. According to the SEM examination, the

NiO NPs were spherical with variable forms and diameters in the range of 100–400 nm (Figure 16a,b). The photodegradation investigation showed that, within 20 min, orange II in aqueous medium was degraded by the NiO NPs and NiO/Nc by 93% and 96%, respectively (Figure 16c). Green methods are successfully applied for preparing NiO as a photocatalyst. For example, using the antioxidant property of *Punica granatum* L. (pomegranate) juice extract and its bio-reducing ability for MO breakdown in water, Barzinjy et al. [140] prepared NiO NPs. The biosynthesized NiO nanoparticles displayed an active catalytic ability toward the degradation of MO from media with a total degradation performance of 96%. Furthermore, Sarani et al. [141] prepared NiO nanoparticles via a green method by using extract as a stabilizing agent. The average crystal size of prepared NiO nanoparticles was approximately 54–58 nm, and the estimated energy band gap was 3–3.7. The prepared NiO nanoparticles were investigated as photocatalysts for degradation of acid orange 7 (AO7) dye in aqueous solution under visible light. The NiO nanoparticles exhibited excellent photocatalytic performance (90.2%) toward the AO7 dye and displayed excellent re-usability several times. Table 1 summarizes different metal oxide morphologies and their photodegradation performances.
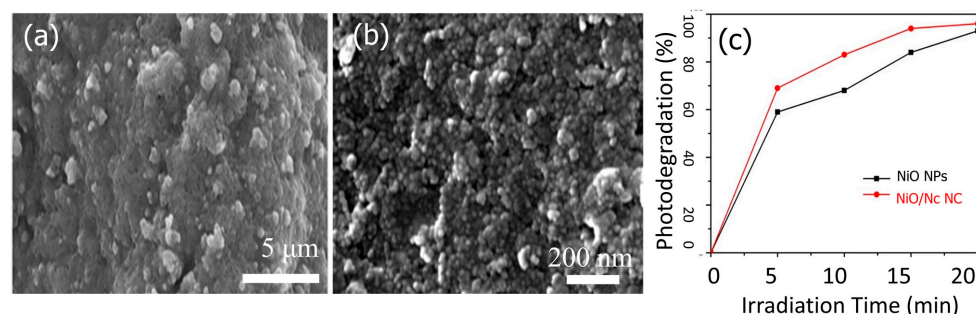

Figure 16. SEM image of (**a**) NiO NPs and (**b**) NiO/Nc composite, and (**c**) percent of degradation for orange II dye. Adopted with permission from Ref. [139] Copyright 2022, Springer Nature.

Table 1. Summary of different metal oxide morphologies and their photodegradation performances.
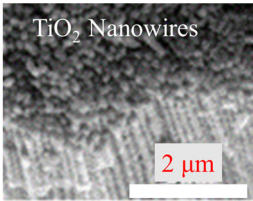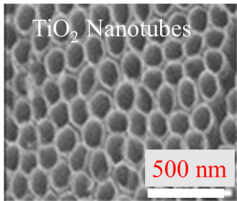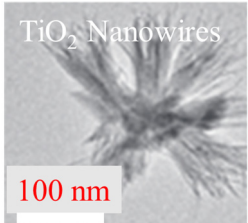
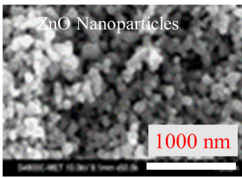| Photocatalyst	Morphology	Pollutant	Degradation Conditions	Degradation Rate (%)	Ref.
TiO$_2$	TiO$_2$ Nanowires 2 μm	MB	UV light Time 80 min Pseudo-first order (k = 0.0098 min^{-1})	75.00	[83]
	TiO$_2$ Nanotubes 500 nm		UV light Time 80 min Pseudo-first order (k = 0.0426 min^{-1})	99.00	[83]
	TiO$_2$ Nanowires 100 nm	RhB	UV light Time 10 min	50.00	[84]

Table 1. *Cont.*
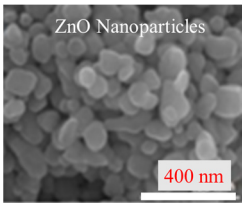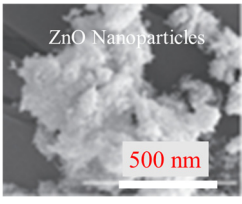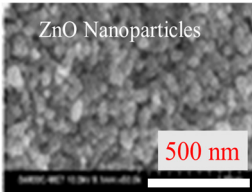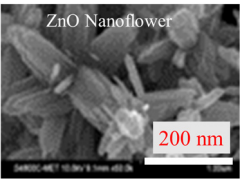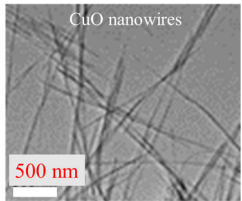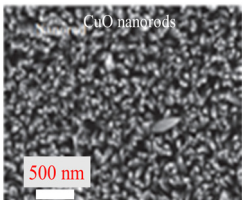
Photocatalyst	Morphology	Pollutant	Degradation Conditions	Degradation Rate (%)	Ref.
ZnO	ZnO Nanoparticles 400 nm	MO	UV light Time 150 min Pseudo-first order (k = 0.01659 cm^{-1})	99.00	[108]
	ZnO Nanoparticles 500 nm	RhB	UV light Time 160 min	95.40	[109]
	ZnO Nanoparticles 500 nm	RhB	UV light Pseudo-first order (k = 0.014 min^{-1})	80.44	[110]
	ZnO Nanoparticles 1000 nm	MG	UV light Pseudo-first order (k = 0.017 min^{-1})	83.68	
	ZnO Nanoflower 200 nm	MG	UV light Pseudo-first order (k = 0.023 min^{-1})	90.87	[110]
CuO	CuO nanowires 500 nm	RhB	UV light Time 9 h	95.00	[129]
	CuO nanorods 500 nm	CR	UV light Time 210 min	67.00	[130]

Table 1. *Cont.*
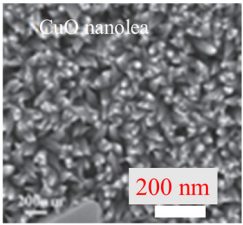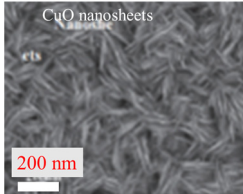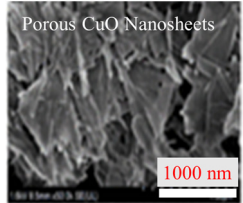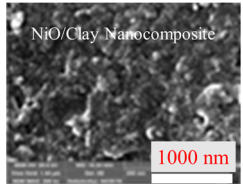
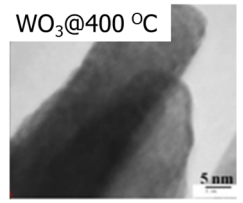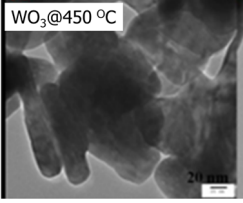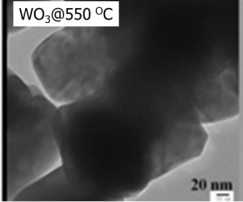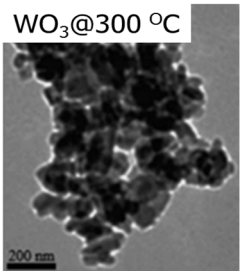| Photocatalyst	Morphology	Pollutant	Degradation Conditions	Degradation Rate (%)	Ref.
CuO	CuO nanolea 200 nm	CR	UV light Time 210 min	48.00	[130]
	CuO nanosheets 200 nm		UV light Time 210 min	12.00	
	Porous CuO Nanosheets 1000 nm	AR	UV-vis light Pseudo-first order ($k = 0.524$ min^{-1})	96.99	[133]
NiO	NiO/Clay Nanocomposite 1000 nm	O II	UV–Vis light Time 20 min	96.00	[139]
WO$_3$	WO$_3$@400 °C 5 nm	MB	UV light Time 160 min	11.00	[142]
	WO$_3$@450 °C 20 nm		UV light Time 16 min	14.30	[142]
	WO$_3$@550 °C 20 nm		UV light Time 160 min	20.00	[142]

Table 1. *Cont.*

Photocatalyst	Morphology	Pollutant	Degradation Conditions	Degradation Rate (%)	Ref.
WO_3	WO₃@300 °C	RhB	Visible light Time 240 min	96.10	[143]

4.5. Tungsten Oxide Photocatalysts

In recent decades, tungsten-based oxides (WO_3) have been the subject of substantial research, with a variety of morphologies being exhibited. A twisted WO_6 octahedron connects the crystal in the stoichiometric ratio of the WO_3 structure to generate a perovskite crystal structure. Its crystal forms are hexagonal, orthorhombic, and monoclinic. At the same time, oxygen vacancies and unsaturated, coordinated W atoms might arise from the easy loss of the oxygen lattice. Consequently, there are numerous non-stoichiometric compounds in tungsten oxide, including $WO_{2.72}$, $WO_{2.8}$, $WO_{2.83}$, and $WO_{2.9}$.

Among the low-cost semiconductors with potential photocatalytic activity is tungsten oxide (WO_3) [56]. Its highly adjustable stoichiometries and structures, together with its Earth-abundance and strong sensitivity to the solar spectrum due to its low band gap of 2.5–3.0 eV [144], make it a popular choice for photocatalysis under visible light [145]. Furthermore, WO_3 has stable physical and chemical characteristics, little toxicity, and a strong capacity to oxidize valence band holes [39]. Nanoparticles, nanowires, nanosheets, and nanospheres are among the frequently occurring morphologies. There are many ways to produce different WO_3 dimensions: 0 dimensional (0D), 1D, 2D, and 3D WO_3, in that order. Characteristics vary among dimensions. It is possible to create 0D WO_3 monodisperse monoclinic WO_3 quantum dots by breaking down the ammonium tungstate oxide complex, which is created hydrothermally using hydrazine hydrate and WCl_6 [146]. It is possible to carefully regulate the particle size distribution of WO_{3-x} QDS within the range of 1.3–4.5 nm by varying the reaction temperature [147]. 1D WO_3 is widely available and simple to synthesize. Today, various structures of 1D WO_3 have been discovered, such as those of nanofibers, nanotubes, nanorods, and nanowires. As for 2D WO_3, thin films, nanosheets, nanoplates, and so on, these have garnered a great deal of interest because of their high surface volume ratio, surface polarization, modulated surface activity, and oxygen-rich vacancies. The majority of 2D WO_3 structures are thin layers. As previously reported by Yin et al., 3D WO_3 is a layered structure made of nanoparticles, nanoplates, nanorods, and nanosheets. It can take the form of irregular structures such as mesoporous structures, microspheres, micro flowers, and sea urchin-like formations. Typically, 3D WO_3 displays high porosity, a large specific surface area, and a distinctive shape [148].

For photocatalytic applications, WO_3 shows some advantages, such as its high physio-chemical catalyst stability that is limited to photo-corrosion and has strong solar spectrum absorption. Under UV–Vis light, WO_3 is a highly reactive catalyst that effectively oxidizes various organic and inorganic pollutants in wastewater. WO_3 is a photocatalyst with a wide range of hues that can change from yellow to green to bluish to grayish depending on its oxidation state. There are many techniques that have been used to enhance the catalytic activity of WO_3. For example, doping with other materials such as dyes to form dye-doped WO_3 as reported by Tahir et al. [149], or doping with Pt to form Pt–WO_3 composite [150].

One of the promising strategies is to design WO_3 with a different morphology, and we will present the recent progress in utilizing WO_3 with different morphologies in degradation some organic dyes. Ojha et al. [142] used the sol-gel method to prepare WO_3 nanorods

and sheets in various crystal phases. As presented in Figure 17a, they showed that the calcination temperature plays a critical role in the shapes and crystal phases of the WO_3 nanostructures, and thus in the photocatalytic activity toward degradation of MB dye due to the modified electronic structure, which causes a variation in the value of the band gap (Figure 17b). The synthesized WO_3 nanosheets showed improved photocatalytic activity for the photodegradation of MB dye compared to WO_3 nanorods (Figure 17c). The sheet-type structure provides more active surface for the interaction of dye molecules compared to the rods.
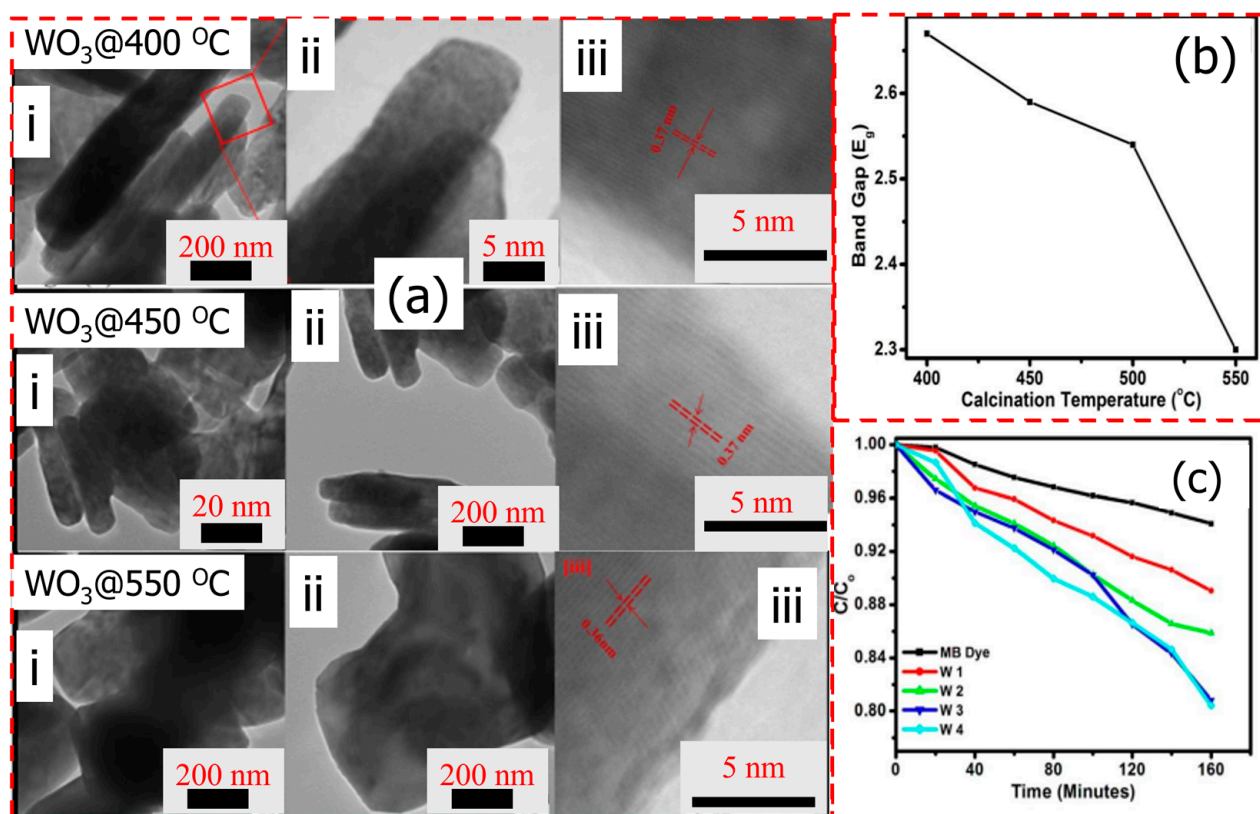

Figure 17. (**a**) TEM images with various resolutions of WO_3 calcined at different temperatures, (**b**) variation in band gap with calcination temperature, and (**c**) C/Co vs. UV irradiation time plot for degradation of MB dye with W1 (at 400 °C), W2 (at 450 °C), W3 (at 550 °C), and W4 (at 550 °C). Adopted with permission from Ref. [142] Copyright 2022, Springer Nature.

Yin et al. [148] prepared WO_3 photocatalyst through a hydrothermal process. The prepared WO_3 nanoparticles showed promising absorption of UV, visible, and near-infrared (NIR) bandwidths. WO_3 photocatalyst exhibited excellent catalytic activity toward the degradation of MB. Furthermore, they confirmed that the temperature showed different morphology (Figure 18a–d) and that the higher temperature displayed better catalytic activity (Figure 18e). Recently, Mzimela et al. [143] prepared highly agglomerated WO_3 nanoparticles through the facile acid precipitation method at various temperature (Figure 18f–h) for degradation of RhB dye. The results showed that WO_3 calcined at 300 °C, 5 g L^{-1} catalyst dose, 5 ppm RhB concentration, and pH of 9.5, while the catalyst showed an excellent degradation efficiency of 96.1% after 4 h under visible light irradiation (Figure 18i). Furthermore, the degradation kinetics obeys the L–H model, which describes heterogenous photocatalytic surface reactions.
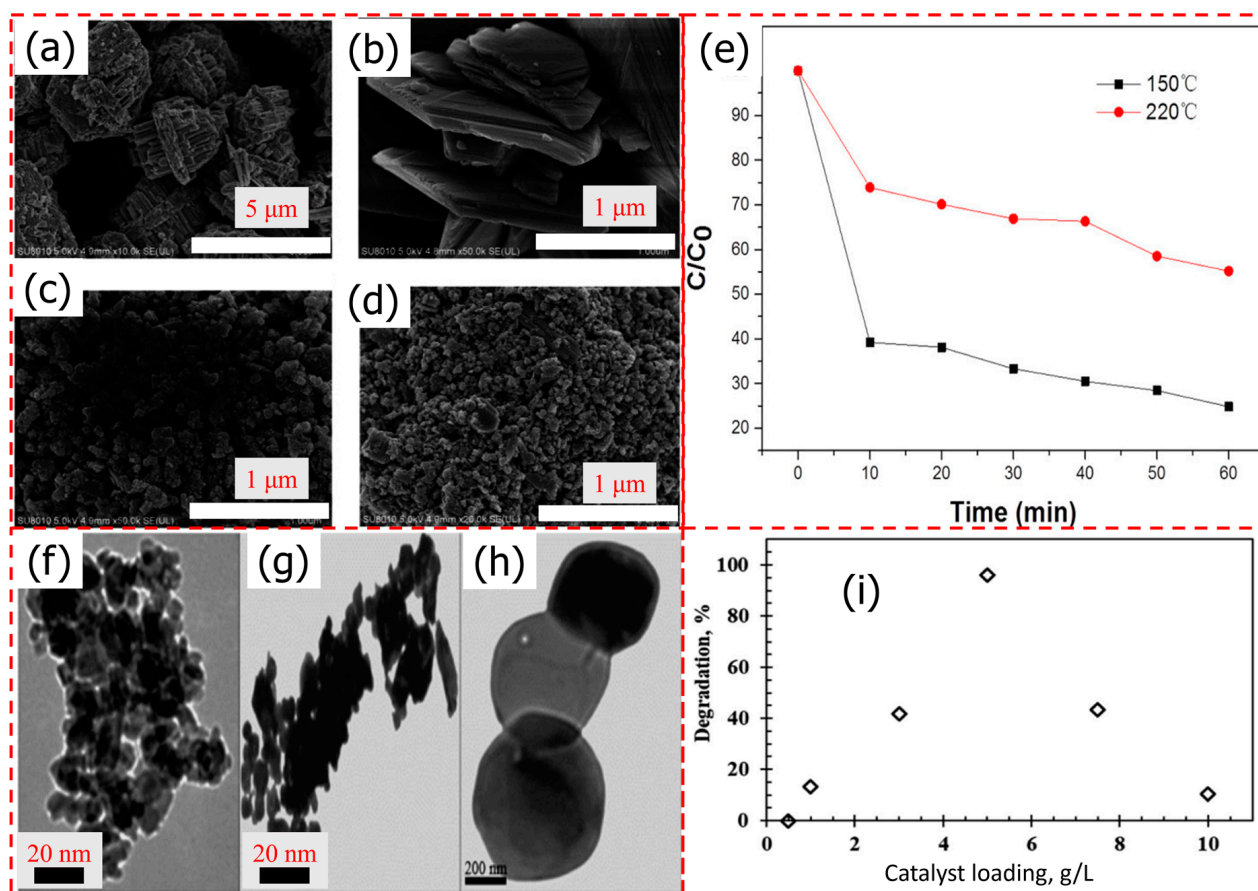
Figure 18. (**a**,**b**) SEM images of WO_3 calcined at 150 °C, and (**c**,**d**) at 220 °C. (**e**) The photodegradation profile of MB in the presence of the WO_3 photocatalyst under NIR laser irradiation. Adopted with permission from Ref. [148] Copyright 2022, Springer Nature. TEM images of WO_3 particles calcined at (**f**) 300 °C, (**g**) 500 °C, and (**h**) 700 °C, and (**i**) effect of catalyst loading on the photocatalytic degradation of RhB at a pH 9.5 and 5 ppm RhB at a calcination temperature of 300 °C. Adopted with permission from Ref. [143] Copyright 2022, Royal Society of Chemistry.

5. Conclusions and Future Perspectives

Due to the industrial revolution in the modern world, various pollutants are emitted into the environment, both directly and indirectly. Thus, great efforts have been devoted to develop advanced technology for the elimination of such environmental pollutants. One of the most promising methods for meeting global needs in an environmentally responsible manner is photocatalysis. Metal oxides are found to be potential photocatalysts because of their affordability, effectiveness, and environmental friendliness. Furthermore, metal oxides may be widely used in a wide range of applications because of their large surface area, simplicity of fabrication, and sufficient supply. Moreover, metal oxides are abundant, highly active, and could be prepared either through eco-friendly or conventional methods in large quantities. Unfortunately, a few drawbacks prevent them from being used practically, including a large bandgap, a high rate of photogenerated electron–hole pair recombination, and catalyst deactivation. Therefore, various strategies have been developed to overcome these limitations; one of these techniques is the design of metal oxides with unique morphologies. The morphology of metal oxides displayed a significant influence on the overall degradation performance, as indicated by shifting the photocatalytic degradation toward various kinds of dyes in aqueous solutions. Therefore, in the current study, the recent progress in the photocatalytic degradation of organic dyes by prominent metal oxides with different morphologies is discussed. The metal oxide nanoparticles, namely, TiO_2, ZnO,

CuO, NiO, and WO_3, all are widely utilized for the photodegradation of various organic dyes. The non-spherical morphologies such as nanorods and nanowires exhibit enhanced photocatalytic performance due to their unique crystal facets and surface areas, which can promote charge transfer and improve catalytic efficiency. Ultimately, the selection of a particular morphology for a photocatalyst relies on the specific application and the desired properties. The porous design and the substantial specific surface area are responsible for the increased photocatalytic activity. On the other hand, the flake-like structure exhibits comparatively lower performance.

In the future, its highly recommended to do more research to more deeply understand the degradation mechanisms of metal oxides with different morphologies. Until now, most of the prepared metal oxides with different morphologies were obtained by using conventional methods on their appropriate precursors. Some of them are toxic or require the use of a high temperature or organic solvents during the procedure, which is not preferred for sustainability. Thus, it is important to find alternative, sustainable methods for preparing these oxides with different morphologies. Presently, there are some studies reporting the preparation of NiO using green methods; however, they are limited in number and need to be more accurate, as well as to prepare other metal oxides such as TiO_2, ZnO, CuO, and WO_3 for organic dye degradation in aqueous solutions.

Author Contributions: G.A.M.A. and A.S.A.A. designed the work and collected the data. A.H.N., A.S.A.A., and T.A.S.E.-N. wrote the main manuscript text. A.S.A.A. and G.A.M.A. prepared the figures. G.A.M.A., N.F.A., and K.F.C. revised and edited the manuscript. All authors have read and agreed to the published version of the manuscript.

Data Availability Statement: Data is contained within the article.

Conflicts of Interest: The authors declare no conflict of interest.

References

1. Maheshwari, K.; Solanki, Y.S.; Ridoy, M.S.H.; Agarwal, M.; Dohare, R.; Gupta, R. Ultrasonic treatment of textile dye effluent utilizing microwave-assisted activated carbon. *Environ. Prog. Sustain. Energy* **2020**, *39*, e13410. [CrossRef]
2. Ali, H. Biodegradation of Synthetic Dyes—A Review. *Water Air Soil Pollut.* **2010**, *213*, 251–273. [CrossRef]
3. Muhammad; Norzahir, S. A review on the water problem associate with organic pollutants derived from phenol, methyl orange, and remazol brilliant blue dyes. *Mater. Today Proc.* **2020**, *31*, A141–A150. [CrossRef]
4. Sharifi, A.; Montazerghaem, L.; Naeimi, A.; Abhari, A.R.; Vafaee, M.; Ali, G.A.M.; Sadegh, H. Investigation of photocatalytic behavior of modified ZnS:Mn/MWCNTs nanocomposite for organic pollutants effective photodegradation. *J. Environ. Manag.* **2019**, *247*, 624–632. [CrossRef] [PubMed]
5. Couto, S.R. Dye removal by immobilised fungi. *Biotechnol. Adv.* **2009**, *27*, 227–235. [CrossRef] [PubMed]
6. Pavithra, K.G.; Senthil Kumar, P.; Jaikumar, V.; Sundar Rajan, P. Removal of colorants from wastewater: A review on sources and treatment strategies. *J. Ind. Eng. Chem.* **2019**, *75*, 1–19. [CrossRef]
7. Solehudin, M.; Sirimahachai, U.; Ali, G.A.M.; Chong, K.F.; Wongnawa, S. One-pot synthesis of isotype heterojunction g-C_3N_4-MU photocatalyst for effective tetracycline hydrochloride antibiotic and reactive orange 16 dye removal. *Adv. Powder Technol.* **2020**, *31*, 1891–1902. [CrossRef]
8. Pathan, A.; Bhatt, S.H.; Vajapara, S.; Bhasin, C.P. Solar Light Induced Photo Catalytic Properties of α-Fe_2O_3 Nanoparticles for Degradation of Methylene Blue Dye. *Int. J. Thin Film Sci. Technol.* **2022**, *11*, 213–224.
9. Pointing, S. Feasibility of bioremediation by white-rot fungi. *Appl. Microbiol. Biotechnol.* **2001**, *57*, 20–33.
10. Chandralata, R. Fungi from marine habitats: An application in bioremediation1 1Contribution No. 3538 of the National Institute of Oceanography. *Mycol. Res.* **2000**, *104*, 1222–1226.
11. Narayan, R.B.; Goutham, R.; Srikanth, B.; Gopinath, K.P. A novel nano-sized calcium hydroxide catalyst prepared from clam shells for the photodegradation of methyl red dye. *J. Environ. Chem. Eng.* **2018**, *6*, 3640–3647. [CrossRef]
12. Pathan, A.; Prajapati, C.G.; Dave, R.P.; Bhasin, C.P. Effective and Feasible Photocatalytic Degradation of Janus Green B dye in Aqueous Media using PbS/CTAB Nanocomposites. *Int. J. Thin Film Sci. Technol.* **2022**, *11*, 245–255.

13. O'Neill, C.; Hawkes, F.R.; Hawkes, D.L.; Lourenço, N.D.; Pinheiro, H.M.; Delée, W. Colour in textile effluents—*Sources*, measurement, discharge consents and simulation: A review. *J. Chem. Technol. & Biotechnol.* **1999**, *74*, 1009–1018.

14. Jin, X.-C.; Liu, G.-Q.; Xu, Z.-H.; Tao, W.-Y. Decolorization of a dye industry effluent by Aspergillus fumigatus XC6. *Appl. Microbiol. Biotechnol.* **2007**, *74*, 239–243. [CrossRef] [PubMed]

15. Maafa, I.M.; Ali, M.A. Enhanced Organic Pollutant Removal Efficiency of Electrospun NiTiO$_3$/TiO$_2$-Decorated Carbon Nanofibers. *Polymers* **2023**, *15*, 109. [CrossRef] [PubMed]

16. Mohamad Amran Mohd, S.; Dalia Khalid, M.; Wan Azlina Wan Abdul, K.; Azni, I. Cationic and anionic dye adsorption by agricultural solid wastes: A comprehensive review. *Desalination* **2011**, *280*, 1–13.

17. Yuxing, W.; Jian, Y. Laccase-catalyzed decolorization of synthetic dyes. *Water Res.* **1999**, *33*, 3512–3520.

18. Esther, F.; Tibor, C.; Gyula, O. Removal of synthetic dyes from wastewaters: A review. *Environ. Int.* **2004**, *30*, 953–971.

19. Pourbabaee, A.A.; Malekzadeh, F.; Sarbolouki, M.N.; Najafi, F. Aerobic Decolorization and Detoxification of a Disperse Dye in Textile Effluent by a New Isolate of *Bacillus* sp. *Biotechnol. Bioeng.* **2006**, *93*, 631–635. [CrossRef]

20. Singh, H. Fungal decolorization and degradation of dyes. In *Mycoremediation: Fungal Bioremediation*; Wiley: Hoboken, NJ, USA, 2006; pp. 420–483.

21. Ahmed, A.S.A.; Sanad, M.M.S.; Kotb, A.; Negm, A.N.R.M.; Abdallah, M.H. Removal of methyl red from wastewater using a NiO@Hyphaene thebaica seed-derived porous carbon adsorbent: Kinetics and isotherm studies. *Mater. Adv.* **2023**, *4*, 2981–2990. [CrossRef]

22. Yuzhu, F.; Viraraghavan, T. Fungal decolorization of dye wastewaters: A review. *Bioresour. Technol.* **2001**, *79*, 251–262.

23. Haoran, D.; Guangming, Z.; Lin, T.; Changzheng, F.; Chang, Z.; Xiaoxiao, H.; Yan, H. An overview on limitations of TiO$_2$-based particles for photocatalytic degradation of organic pollutants and the corresponding countermeasures. *Water Res.* **2015**, *79*, 128–146.

24. Xi, Z.; Jing, W.; Xing-Xing, D.; Yun-Kai, L. Functionalized metal-organic frameworks for photocatalytic degradation of organic pollutants in environment. *Chemosphere* **2020**, *242*, 125144.

25. Pelizzetti, E.; Minero, C. Metal Oxides as Photocatalysts for Environmental Detoxification. *Comments Inorg. Chem.* **1993**, *15*, 297–337. [CrossRef]

26. Li, L.; Zhong, Y.; Hu, Y.; Bai, J.; Qiao, F.; Ahmed, A.S.A.; Ali, G.; Zhao, X.; Xie, Y. Room-temperature synthesis of Ag- and Mn-doped Cs$_2$NaBiCl$_6$ octahedrons for dye photodegradation. *CrystEngComm* **2023**, *25*, 4355–4363. [CrossRef]

27. Nigora, T.; Irma, K. Effects of electronic structure of catalytic nanoparticles on carbon nanotube growth. *Carbon Trends* **2021**, *5*, 100092.

28. Muhammad Sohail, B.; Naveed, R.; Tayyaba, N.; Ghulam, A.; Xiangling, G.; Muhammad, A.; Muhammad, Q.; Humaira, B.; Syed Shoaib Ahmad, S.; Mika, S. Metallic nanoparticles for catalytic reduction of toxic hexavalent chromium from aqueous medium: A state-of-the-art review. *Sci. Total Environ.* **2022**, *829*, 154475.

29. Chen, H.; Nanayakkara, C.E.; Grassian, V.H. Titanium Dioxide Photocatalysis in Atmospheric Chemistry. *Chem. Rev.* **2012**, *112*, 5919–5948. [CrossRef]

30. Ansari, S.A.; Khan, M.M.; Kalathil, S.; Nisar, A.; Lee, J.; Cho, M.H. Oxygen vacancy induced band gap narrowing of ZnO nanostructures by an electrochemically active biofilm. *Nanoscale* **2013**, *5*, 9238–9246. [CrossRef]

31. Wang, H.; Rogach, A.L. Hierarchical SnO$_2$ Nanostructures: Recent Advances in Design, Synthesis, and Applications. *Chem. Mater.* **2014**, *26*, 123–133. [CrossRef]

32. Sun, C.; Li, H.; Chen, L. Nanostructured ceria-based materials: Synthesis, properties, and applications. *Energy Environ. Sci.* **2012**, *5*, 8475–8505. [CrossRef]

33. Oturan, M.A.; Aaron, J.J. Advanced Oxidation Processes in Water/Wastewater Treatment: Principles and Applications. A Review. *Crit. Rev. Environ. Sci. Technol.* **2014**, *44*, 2577–2641. [CrossRef]

34. Rauf, M.A.; Meetani, M.A.; Hisaindee, S. An overview on the photocatalytic degradation of azo dyes in the presence of TiO$_2$ doped with selective transition metals. *Desalination* **2011**, *276*, 13–27. [CrossRef]

35. Laouini, S.E.; Bouafia, A.; Soldatov, A.V.; Algarni, H.; Tedjani, M.L.; Ali, G.A.M.; Barhoum, A. Green Synthesized of Ag/Ag$_2$O Nanoparticles Using Aqueous Leaves Extracts of Phoenix dactylifera L. and Their Azo Dye Photodegradation. *Membranes* **2021**, *11*, 468. [CrossRef] [PubMed]

36. Mohammad Mansoob, K.; Syed Farooq, A.; Abdullah, A.-M. Metal oxides as photocatalysts. *J. Saudi Chem. Soc.* **2015**, *19*, 462–464.

37. Moniz, S.J.A.; Zhu, J.; Tang, J. 1D Co-Pi Modified BiVO$_4$/ZnO Junction Cascade for Efficient Photoelectrochemical Water Cleavage. *Adv. Energy Mater.* **2014**, *4*, 1301590. [CrossRef]

38. Rauf, M.A.; Ashraf, S.; Alhadrami, S.N. Photolytic oxidation of Coomassie Brilliant Blue with H$_2$O$_2$. *Dye. Pigment.* **2005**, *66*, 197–200. [CrossRef]

39. Theerthagiri, J.; Chandrasekaran, S.; Salla, S.; Elakkiya, V.; Senthil, R.; Nithyadharseni, P.; Maiyalagan, T.; Micheal, K.; Ayeshamariam, A.; Arasu, M.V. Recent developments of metal oxide based heterostructures for photocatalytic applications towards environmental remediation. *J. Solid State Chem.* **2018**, *267*, 35–52. [CrossRef]

40. Danish, M.S.; Estrella, L.L.; Alemaida, I.M.A.; Lisin, A.; Moiseev, N.; Ahmadi, M.; Nazari, M.; Wali, M.; Zaheb, H.; Senjyu, T. Photocatalytic Applications of Metal Oxides for Sustainable Environmental Remediation. *Metals* **2021**, *11*, 80. [CrossRef]

41. Asma, R.; Muhammad, I.; Ali, S.; Faiza, N.; Maaz, K.; Qasim, K.; Muhammad, M. Photocatalytic degradation of dyes using semiconductor photocatalysts to clean industrial water pollution. *J. Ind. Eng. Chem.* **2021**, *97*, 111–128.

42. Ajmal, A.; Majeed, I.; Malik, R.N.; Idriss, H.; Nadeem, M.A. Principles and mechanisms of photocatalytic dye degradation on TiO$_2$ based photocatalysts: A comparative overview. *RSC Adv.* **2014**, *4*, 37003–37026. [CrossRef]

43. Ioannis, K.K.; Triantafyllos, A.A. TiO$_2$-assisted photocatalytic degradation of azo dyes in aqueous solution: Kinetic and mechanistic investigations: A review. *Appl. Catal. B Environ.* **2004**, *49*, 1–14.

44. Meng, A.; Zhou, S.; Wen, D.; Han, P.; Su, Y. g-C$_3$N$_4$/CoTiO$_3$ S-scheme heterojunction for enhanced visible light hydrogen production through photocatalytic pure water splitting. *Chin. J. Catal.* **2022**, *43*, 2548–2557. [CrossRef]

45. Alvarez-Ramirez, J.; Femat, R.; Meraz, M.; Ibarra-Valdez, C. Some remarks on the Langmuir–Hinshelwood kinetics. *J. Math. Chem.* **2016**, *54*, 375–392. [CrossRef]

46. Tran, H.D.; Nguyen, D.Q.; Do, P.T.; Tran, U.N.P. Kinetics of photocatalytic degradation of organic compounds: A mini-review and new approach. *RSC Adv.* **2023**, *13*, 16915–16925. [CrossRef]

47. Barkha, R.; Arpan Kumar, N.; Niroj Kumar, S. Fundamentals principle of photocatalysis. In *Micro and Nano Technologies*; Elsevier: Amsterdam, The Netherlands, 2022; pp. 1–22. [CrossRef]

48. Kumar, K.V.; Porkodi, K.; Rocha, F. Langmuir–Hinshelwood kinetics—A theoretical study. *Catal. Commun.* **2008**, *9*, 82–84. [CrossRef]

49. Swenson, H.; Stadie, N.P. Langmuir's Theory of Adsorption: A Centennial Review. *Langmuir* **2019**, *35*, 5409–5426. [CrossRef]

50. Sun, P.; Zhang, J.; Liu, W.; Wang, Q.; Cao, W. Modification to L-H Kinetics Model and Its Application in the Investigation on Photodegradation of Gaseous Benzene by Nitrogen-Doped TiO$_2$. *Catalysts* **2018**, *8*, 326. [CrossRef]

51. Zhan, X.; Yan, C.; Zhang, Y.; Rinke, G.; Rabsch, G.; Klumpp, M.; Schäfer, A.I.; Dittmeyer, R. Investigation of the reaction kinetics of photocatalytic pollutant degradation under defined conditions with inkjet-printed TiO$_2$ films—*From* batch to a novel continuous-flow microreactor. *React. Chem. Eng.* **2020**, *5*, 1658–1670. [CrossRef]

52. Huang, C.; Chen, L.; Li, H.; Mu, Y.; Yang, Z. Synthesis and application of Bi$_2$WO$_6$ for the photocatalytic degradation of two typical fluoroquinolones under visible light irradiation. *RSC Adv.* **2019**, *9*, 27768–27779. [CrossRef]

53. Amir, Z.; Muhammad, K.; Muhammad Asim, K.; Qasim, K.; Aziz, H.-Y.; Alei, D.; Muhammad, M. Review on the hazardous applications and photodegradation mechanisms of chlorophenols over different photocatalysts. *Environ. Res.* **2021**, *195*, 110742.

54. Yue, B.; Zhou, Y.; Xu, J.; Wu, Z.; Zhang, X.; Zou, Y.; Jin, S. Photocatalytic Degradation of Aqueous 4-Chlorophenol by Silica-Immobilized Polyoxometalates. *Environ. Sci. Technol.* **2002**, *36*, 1325–1329. [CrossRef] [PubMed]

55. Kumar, K.V.A.; Chandana, L.; Ghosal, P.; Ch, S. Simultaneous photocatalytic degradation of p-cresol and Cr (VI) by metal oxides supported reduced graphene oxide. *Mol. Catal.* **2018**, *451*, 87–95. [CrossRef]

56. Naeimi, A.; Sharifi, A.; Montazerghaem, L.; Abhari, A.R.; Mahmoodi, Z.; Bakr, Z.H.; Soldatov, A.V.; Ali, G.A.M. Transition metals doped WO$_3$ photocatalyst towards high efficiency decolourization of azo dye. *J. Mol. Struct.* **2022**, *1250*, 131800. [CrossRef]

57. Hisatomi, T.; Kubota, J.; Domen, K. Recent advances in semiconductors for photocatalytic and photoelectrochemical water splitting. *Chem. Soc. Rev.* **2014**, *43*, 7520–7535. [CrossRef] [PubMed]

58. Hoffmann, M.R.; Martin, S.T.; Choi, W.; Bahnemann, D.W. Environmental Applications of Semiconductor Photocatalysis. *Chem. Rev.* **1995**, *95*, 69–96. [CrossRef]

59. Fujishima, A.; Honda, K. Electrochemical Photolysis of Water at a Semiconductor Electrode. *Nature* **1972**, *238*, 37–38. [CrossRef]

60. Ryu, A. Recent progress on photocatalytic and photoelectrochemical water splitting under visible light irradiation. *J. Photochem. Photobiol. C Photochem. Rev.* **2010**, *11*, 179–209.

61. Inoue, T.; Fujishima, A.; Konishi, S.; Honda, K. Photoelectrocatalytic reduction of carbon dioxide in aqueous suspensions of semiconductor powders. *Nature* **1979**, *277*, 637–638. [CrossRef]

62. Kazuya, N.; Akira, F. TiO$_2$ photocatalysis: Design and applications. *J. Photochem. Photobiol. C Photochem. Rev.* **2012**, *13*, 169–189.

63. Dahl, M.; Liu, Y.; Yin, Y. Composite Titanium Dioxide Nanomaterials. *Chem. Rev.* **2014**, *114*, 9853–9889. [CrossRef] [PubMed]

64. Ethiraj, A.S.; Rhen, D.S.; Soldatov, A.V.; Ali, G.A.M.; Bakr, Z.H. Efficient and recyclable Cu incorporated TiO$_2$ nanoparticle catalyst for organic dye photodegradation. *Int. J. Thin Film Sci. Technol.* **2021**, *10*, 169–182.

65. Bajpai, S.; Tiwary, S.K.; Sonker, M.; Joshi, A.; Gupta, V.; Kumar, Y.; Shreyash, N.; Biswas, S. Recent Advances in Nanoparticle-Based Cancer Treatment: A Review. *ACS Appl. Nano Mater.* **2021**, *4*, 6441–6470. [CrossRef]

66. Giahi, M.; Pathania, D.; Agarwal, S.; Ali, G.A.M.; Chong, K.F.; Gupta, V.K. Preparation of Mg-doped TiO$_2$ nanoparticles for photocatalytic degradation of some organic pollutants. *Stud. Univ. Babes-Bolyai Chem.* **2019**, *64*, 7–18. [CrossRef]

67. Nair, A.; PonnanEttiyappan, J. Ag–TiO$_2$ Nanofiber Membranes for Photocatalytic Degradation of Dyes. *Adv. Sci. Lett.* **2018**, *24*, 5764–5767. [CrossRef]

68. Nair, A.K.; JagadeeshBabu, P.E. TiO$_2$ nanosheet-graphene oxide based photocatalytic hierarchical membrane for water purification. *Surf. Coat. Technol.* **2017**, *320*, 259–262. [CrossRef]

69. Tomoaki, T.; Haruka, N.; Motoki, M.; Akihide, I.; Akihiko, K. Photocatalytic CO$_2$ reduction using water as an electron donor over Ag-loaded metal oxide photocatalysts consisting of several polyhedra of Ti^{4+}, Zr^{4+}, and Ta^{5+}. *J. Photochem. Photobiol. A Chem.* **2018**, *358*, 416–421.

70. Wang, R.; Hashimoto, K.; Fujishima, A.; Chikuni, M.; Kojima, E.; Kitamura, A.; Shimohigoshi, M.; Watanabe, T. Light-induced amphiphilic surfaces. *Nature* **1997**, *388*, 431–432. [CrossRef]

71. Ye, S.; Sun, H.; Wu, J.; Wan, L.; Ni, Y.; Wang, R.; Xiang, Z.; Deng, X. Supercritical CO$_2$ Assisted TiO$_2$ Preparation to Improve the UV Resistance Properties of Cotton Fiber. *Polymers* **2022**, *14*, 5513. [CrossRef]

72. Bahareh Ghorbani, A.; Neda, G.; Javad Vahabzade, P.; Azadeh Ebrahimian, P. Boosting the photoconversion efficiency of TiO₂ nanotubes using UV radiation-assisted anodization as a prospective method: An efficient photocatalyst for eliminating resistant organic pollutants. *Ceram. Int.* **2020**, *46*, 19942–19951.

73. Reza, A.; Ali Reza, M.; Lotf Ali, S.; Soheila, S. Characterization and optical properties of spherical WO₃ nanoparticles synthesized via the reverse microemulsion process and their photocatalytic behavior. *Mater. Lett.* **2014**, *133*, 208–211.

74. Bai, H.; Liu, Z.; Sun, D.D. Hierarchically multifunctional TiO₂ nano-thorn membrane for water purification. *Chem. Commun.* **2010**, *46*, 6542–6544. [CrossRef] [PubMed]

75. Liu, B.; Nakata, K.; Sakai, M.; Saito, H.; Ochiai, T.; Murakami, T.; Takagi, K.; Fujishima, A. Mesoporous TiO₂ Core–Shell Spheres Composed of Nanocrystals with Exposed High-Energy Facets: Facile Synthesis and Formation Mechanism. *Langmuir* **2011**, *27*, 8500–8508. [CrossRef] [PubMed]

76. Ata, U.; Lutfur, R.; Syed Zajif, H.; Wasim, A.; Abdul, T.; Asim, J.; Sadia Zafar, B.; Waheed, S.K.; Rabia, R.; Irshad, H.; et al. Mechanistic insight of dye degradation using TiO₂ anchored α-MnO₂ nanorods as promising sunlight driven photocatalyst. *Mater. Sci. Eng. B* **2021**, *271*, 115257.

77. Sarah Mozzaquatro, P.; Alexsandra, V.; Guilin, Y.; Jingfeng, W.; Selene, M.A.G.U.; Dachamir, H.; Antônio Augusto, U. An overview on nanostructured TiO₂–containing fibers for photocatalytic degradation of organic pollutants in wastewater treatment. *J. Water Process Eng.* **2021**, *40*, 101827.

78. Thammasak, R.; Orawan, R.; Sanya, S.; Sivakorn, A. Application of TiO₂ nanotubes as photocatalysts for decolorization of synthetic dye wastewater. *Water Resour. Ind.* **2021**, *26*, 100163.

79. Lee, S.Y.; Kang, D.; Jeong, S.; Do, H.T.; Kim, J.H. Photocatalytic Degradation of Rhodamine B Dye by TiO₂ and Gold Nanoparticles Supported on a Floating Porous Polydimethylsiloxane Sponge under Ultraviolet and Visible Light Irradiation. *ACS Omega* **2020**, *5*, 4233–4241. [CrossRef] [PubMed]

80. Yao, L.; Haas, T.W.; Guiseppi-Elie, A.; Bowlin, G.L.; Simpson, D.G.; Wnek, G.E. Electrospinning and stabilization of fully hydrolyzed poly (vinyl alcohol) fibers. *Chem. Mater.* **2003**, *15*, 1860–1864. [CrossRef]

81. Katsumata, K.-i.; Okazaki, S.; Cordonier, C.E.J.; Shichi, T.; Sasaki, T.; Fujishima, A. Preparation and Characterization of Self-Cleaning Glass for Vehicle with Niobia Nanosheets. *ACS Appl. Mater. Interfaces* **2010**, *2*, 1236–1241. [CrossRef]

82. Zhang, M.; Wang, C.; Wang, Y.; Li, S.; Zhang, X.; Liu, Y. Tunable bismuth doping/loading endows NaTaO₃ nanosheet highly selective photothermal reduction of CO₂. *Nano Res.* **2023**, *16*, 2142–2151. [CrossRef]

83. Zhen, J.; Fan-Li, M.; Yong, J.; Tao, L.; Jin-Yun, L.; Bai, S.; Jin, W.; Jin-Huai, L.; Xing-Jiu, H. Porous TiO₂ nanowires derived from nanotubes: Synthesis, characterzation and their enhanced photocatalytic properties. *Microporous Mesoporous Mater.* **2013**, *181*, 146–153.

84. Wu, H.B.; Hng, H.H.; Lou, X.W. Direct Synthesis of Anatase TiO₂ Nanowires with Enhanced Photocatalytic Activity. *Adv. Mater.* **2012**, *24*, 2567–2571. [CrossRef] [PubMed]

85. Sadaf Bashir, K.; Mengjing, H.; Shuang, S.; Zhengjun, Z. Morphological influence of TiO₂ nanostructures (nanozigzag, nanohelics and nanorod) on photocatalytic degradation of organic dyes. *Appl. Surf. Sci.* **2017**, *400*, 184–193.

86. Krishnamoorthy, S.; Ronen, B.-Z.; Orit, M.; Tomer, Z. Controllable synthesis of TiO₂ nanoparticles and their photocatalytic activity in dye degradation. *Mater. Res. Bull.* **2020**, *126*, 110842.

87. Saba, H.; Masoud, J. Synthesis of TiO₂ nanoparticles coated on cellulose nanofibers with different morphologies: Effect of the template and sol-gel parameters. *Mater. Sci. Semicond. Process.* **2020**, *109*, 104927.

88. Gihoon, C.; Patrik, S.; Marco, A. Anodic TiO₂ nanotube membranes: Site-selective Pt-activation and photocatalytic H2 evolution. *Electrochim. Acta* **2017**, *258*, 302–310.

89. Macak, J.M.; Tsuchiya, H.; Taveira, L.; Aldabergerova, S.; Schmuki, P. Smooth Anodic TiO₂ Nanotubes. *Angew. Chem. Int. Ed.* **2005**, *44*, 7463–7465. [CrossRef]

90. Kar, A.; Smith, Y.R.; Subramanian, V. Improved Photocatalytic Degradation of Textile Dye Using Titanium Dioxide Nanotubes Formed Over Titanium Wires. *Environ. Sci. Technol.* **2009**, *43*, 3260–3265. [CrossRef]

91. Kowaka, Y.; Nozaki, K.; Mihara, T.; Yamashita, K.; Miura, H.; Tan, Z.; Ohara, S. Development of TiO₂ Nanosheets with High Dye Degradation Performance by Regulating Crystal Growth. *Materials* **2023**, *16*, 1229. [CrossRef]

92. Nair, A.K.; Roy George, D.; Jos Baby, N.; Reji, M.; Joseph, S. Solar dye degradation using TiO₂ nanosheet based nanocomposite floating photocatalyst. *Mater. Today Proc.* **2021**, *46*, 2747–2751. [CrossRef]

93. Faisal, S.; Jan, H.; Shah, S.A.; Shah, S.; Khan, A.; Akbar, M.T.; Rizwan, M.; Jan, F.; Wajidullah; Akhtar, N.; et al. Green Synthesis of Zinc Oxide (ZnO) Nanoparticles Using Aqueous Fruit Extracts of Myristica fragrans: Their Characterizations and Biological and Environmental Applications. *ACS Omega* **2021**, *6*, 9709–9722. [CrossRef] [PubMed]

94. Manikanika; Lalita, C. Photocatalytic activity of zinc oxide for dye and drug degradation: A review. *Mater. Today Proc.* **2022**, *52*, 1653–1656. [CrossRef]

95. Uribe-López, M.C.; Hidalgo-López, M.C.; López-González, R.; Frías-Márquez, D.M.; Núñez-Nogueira, G.; Hernández-Castillo, D.; Alvarez-Lemus, M.A. Photocatalytic activity of ZnO nanoparticles and the role of the synthesis method on their physical and chemical properties. *J. Photochem. Photobiol. A Chem.* **2021**, *404*, 112866. [CrossRef]

96. Borysiewicz, M.A. ZnO as a Functional Material, a Review. *Crystals* **2019**, *9*, 505. [CrossRef]

97. Ewelina, G.; Martyna, M.; Marta, P.-G.; Adriana, Z.-M. Metal oxide photocatalysts. In *Metal Oxides*; Elsevier: Amsterdam, The Netherlands, 2018; pp. 51–209. [CrossRef]

98. Sotirios, B.; Panayotis, G.; Spyros, N.Y.; Vassilios, D.; Lajos, T.; Athanassios, C.; Nikolaos, B. Preparation of ZnO nanoparticles by thermal decomposition of zinc alginate. *Thin Solid Film.* **2007**, *515*, 8461–8464.

99. Yin, X.; Wang, B.; He, M.; He, T. Facile synthesis of ZnO nanocrystals via a solid state reaction for high performance plastic dye-sensitized solar cells. *Nano Res.* **2012**, *5*, 1–10. [CrossRef]

100. Hasnidawani, J.N.; Azlina, H.N.; Norita, H.; Bonnia, N.N.; Ratim, S.; Ali, E.S. Synthesis of ZnO Nanostructures Using Sol-Gel Method. *Procedia Chem.* **2016**, *19*, 211–216. [CrossRef]

101. Singh, A.K.; Viswanath, V.; Janu, V.C. Synthesis, effect of capping agents, structural, optical and photoluminescence properties of ZnO nanoparticles. *J. Lumin.* **2009**, *129*, 874–878. [CrossRef]

102. Clament Sagaya Selvam, N.; Vijaya, J.J.; Kennedy, L.J. Effects of Morphology and Zr Doping on Structural, Optical, and Photocatalytic Properties of ZnO Nanostructures. *Ind. Eng. Chem. Res.* **2012**, *51*, 16333–16345. [CrossRef]

103. Xu, L.; Hu, Y.-L.; Pelligra, C.; Chen, C.-H.; Jin, L.; Huang, H.; Sithambaram, S.; Aindow, M.; Joesten, R.; Suib, S.L. ZnO with Different Morphologies Synthesized by Solvothermal Methods for Enhanced Photocatalytic Activity. *Chem. Mater.* **2009**, *21*, 2875–2885. [CrossRef]

104. Sakthivel, S.; Neppolian, B.; Shankar, M.V.; Arabindoo, B.; Palanichamy, M.; Murugesan, V. Solar photocatalytic degradation of azo dye: Comparison of photocatalytic efficiency of ZnO and TiO$_2$. *Sol. Energy Mater. Sol. Cells* **2003**, *77*, 65–82. [CrossRef]

105. Ramesh, V.; Raja, S.; Pugazhendhi, A.; Thivaharan, V. Synthesis, characterization and photocatalytic dye degradation capability of Calliandra haematocephala-mediated zinc oxide nanoflowers. *J. Photochem. Photobiol. B Biol.* **2020**, *203*, 111760.

106. Kian Mun, L.; Chin Wei, L.; Koh Sing, N.; Joon Ching, J. Recent developments of zinc oxide based photocatalyst in water treatment technology: A review. *Water Res.* **2016**, *88*, 428–448.

107. Gerischer, H. Electrochemical behavior of semiconductors under illumination. *J. Electrochem. Soc.* **1966**, *113*, 1174. [CrossRef]

108. Sonik, B.; Neha, V. Photocatalytic activity of ZnO nanoparticles with optimization of defects. *Mater. Res. Bull.* **2017**, *95*, 468–476.

109. Dodoo-Arhin, D.; Asiedu, T.; Agyei-Tuffour, B.; Nyankson, E.; Obada, D.; Mwabora, J.M. Photocatalytic degradation of Rhodamine dyes using zinc oxide nanoparticles. *Mater. Today Proc.* **2021**, *38*, 809–815. [CrossRef]

110. Lakshi, S.; Diganta, B.; Mrinal, S.; Banajit, M.; Dipak Kumar, D.; Pinaki, S. Photocatalytic performance of ZnO nanomaterials for self sensitized degradation of malachite green dye under solar light. *Appl. Catal. A Gen.* **2015**, *490*, 42–49.

111. Jing, W.; Yi, X.; Yan, D.; Ruosong, C.; Lan, X.; Sridhar, K. Defect-rich ZnO nanosheets of high surface area as an efficient visible-light photocatalyst. *Appl. Catal. B Environ.* **2016**, *192*, 8–16.

112. Le Pivert, M.; Poupart, R.; Capochichi-Gnambodoe, M.; Martin, N.; Leprince-Wang, Y. Direct growth of ZnO nanowires on civil engineering materials: Smart materials for supported photodegradation. *Microsyst. Nanoeng.* **2019**, *5*, 57. [CrossRef]

113. Kiwaan, H.A.; Atwee, T.M.; Azab, E.A.; El-Bindary, A.A. Efficient photocatalytic degradation of Acid Red 57 using synthesized ZnO nanowires. *J. Chin. Chem. Soc.* **2019**, *66*, 89–98. [CrossRef]

114. Wang, H.; Cai, Y.; Wang, C.; Xu, H.; Fang, J.; Yang, Y. Seeded growth of ZnO nanowires in dye-containing solution: The submerged plant analogy and its application in photodegradation of dye pollutants. *CrystEngComm* **2020**, *22*, 4154–4161. [CrossRef]

115. Dhineshbabu, N.R.; Rajendran, V.; Nithyavathy, N.; Vetumperumal, R. Study of structural and optical properties of cupric oxide nanoparticles. *Appl. Nanosci.* **2016**, *6*, 933–939. [CrossRef]

116. Murali, D.S.; Aryasomayajula, S. Thermal conversion of Cu$_4$O$_3$ into CuO and Cu$_2$O and the electrical properties of magnetron sputtered Cu$_4$O$_3$ thin films. *Appl. Phys. A* **2018**, *124*, 279. [CrossRef]

117. Wang, Y.; Lany, S.; Ghanbaja, J.; Fagot-Revurat, Y.; Chen, Y.P.; Soldera, F.; Horwat, D.; Mücklich, F.; Pierson, J.F. Electronic structures of Cu$_2$O, Cu$_4$O$_3$, and CuO: A joint experimental and theoretical study. *Phys. Rev. B* **2016**, *94*, 245418. [CrossRef]

118. Weldegebrieal, G.K. Photocatalytic and antibacterial activityof CuO nanoparticles biosynthesized using Verbascum thapsus leaves extract. *Optik* **2020**, *204*, 164230. [CrossRef]

119. Phang, Y.-K.; Aminuzzaman, M.; Akhtaruzzaman, M.; Muhammad, G.; Ogawa, S.; Watanabe, A.; Tey, L.-H. Green Synthesis and Characterization of CuO Nanoparticles Derived from Papaya Peel Extract for the Photocatalytic Degradation of Palm Oil Mill Effluent (POME). *Sustainability* **2021**, *13*, 796. [CrossRef]

120. Akintelu, S.A.; Folorunso, A.S.; Folorunso, F.A.; Oyebamiji, A.K. Green synthesis of copper oxide nanoparticles for biomedical application and environmental remediation. *Heliyon* **2020**, *6*, e04508. [CrossRef]

121. Liu, J.; Jin, J.; Deng, Z.; Huang, S.Z.; Hu, Z.Y.; Wang, L.; Wang, C.; Chen, L.-H.; Li, Y.; Tendeloo, G.V.; et al. Tailoring CuO nanostructures for enhanced photocatalytic property. *J. Colloid Interface Sci.* **2012**, *384*, 1–9. [CrossRef]

122. Lufeng, Y.; Deqing, C.; Limin, W. CuO core–shell nanostructures: Precursor-mediated fabrication and visible-light induced photocatalytic degradation of organic pollutants. *Powder Technol.* **2016**, *287*, 346–354.

123. Chiang, C.-Y.; Kosi, A.; Nicholas, F.; Vibha Rani, S.; Sahab, D.; Sheryl, E. Copper oxide nanoparticle made by flame spray pyrolysis for photoelectrochemical water splitting—Part II. Photoelectrochemical study. *Int. J. Hydrog. Energy* **2011**, *36*, 15519–15526. [CrossRef]

124. Sapkota, K.P.; Lee, I.; Hanif, M.A.; Islam, M.A.; Akter, J.; Hahn, J.R. Enhanced Visible-Light Photocatalysis of Nanocomposites of Copper Oxide and Single-Walled Carbon Nanotubes for the Degradation of Methylene Blue. *Catalysts* **2020**, *10*, 297. [CrossRef]

125. Latif, S.; Abdulaziz, F.; Alanazi, A.M.; Alsehli, A.H.; Alsowayigh, M.M.; Alanazi, A.A. Effect of H$_2$O$_2$ @CuONPs in the UV Light-Induced Removal of Organic Pollutant Congo Red Dye: Investigation into Mechanism with Additional Biomedical Study. *Molecules* **2023**, *28*, 410. [CrossRef]

126. Miyauchi, M.; Nakajima, A.; Watanabe, T.; Hashimoto, K. Photocatalysis and Photoinduced Hydrophilicity of Various Metal Oxide Thin Films. *Chem. Mater.* **2002**, *14*, 2812–2816. [CrossRef]

127. Yang, M.; He, J. Fine tuning of the morphology of copper oxide nanostructures and their application in ambient degradation of methylene blue. *J. Colloid Interface Sci.* **2011**, *355*, 15–22. [CrossRef]

128. Zhang, W.; Yang, Z.; Wang, X.; Zhang, Y.; Wen, X.; Yang, S. Large-scale synthesis of β-MnO$_2$ nanorods and their rapid and efficient catalytic oxidation of methylene blue dye. *Catal. Commun.* **2006**, *7*, 408–412. [CrossRef]

129. Wang, L.; Zhou, Q.; Zhang, G.; Liang, Y.; Wang, B.; Zhang, W.; Lei, B.; Wang, W. A facile room temperature solution-phase route to synthesize CuO nanowires with enhanced photocatalytic performance. *Mater. Lett.* **2012**, *74*, 217–219. [CrossRef]

130. Sadollahkhani, A.; Hussain Ibupoto, Z.; Elhag, S.; Nur, O.; Willander, M. Photocatalytic properties of different morphologies of CuO for the degradation of Congo red organic dye. *Ceram. Int.* **2014**, *40*, 11311–11317. [CrossRef]

131. Rao, M.P.; Wu, J.J.; Syed, A.; Ameen, F.; Anandan, S. Synthesis of Dandelion—Like CuO microspheres for photocatalytic degradation of reactive black-5. *Mater. Res. Express* **2018**, *5*, 015053. [CrossRef]

132. George, A.; Raj DM, A.; Venci, X.; Raj, A.D.; Irudayaraj, A.A.; Josephine, R.L.; Kaviyarasu, K. Photocatalytic effect of CuO nanoparticles flower-like 3D nanostructures under visible light irradiation with the degradation of methylene blue (MB) dye for environmental application. *Environ. Res.* **2022**, *203*, 111880. [CrossRef]

133. Nazim, M.; Khan, A.A.P.; Asiri, A.M.; Kim, J.H. Exploring Rapid Photocatalytic Degradation of Organic Pollutants with Porous CuO Nanosheets: Synthesis, Dye Removal, and Kinetic Studies at Room Temperature. *ACS Omega* **2021**, *6*, 2601–2612. [CrossRef]

134. Adawiya, J.H.; Riyad; Hiba, M.S.; Mohammed, J.H. Photocatalytic Activity of Nickel Oxide. *J. Mater. Res. Technol.* **2019**, *8*, 2802–2808.

135. Ahmed, A.S.A.; Xiang, W.; Abdelmotalleib, M.; Zhao, X. Efficient NiO Impregnated Walnut Shell-Derived Carbon for Dye-Sensitized Solar Cells. *ACS Appl. Electron. Mater.* **2022**, *4*, 1063–1071. [CrossRef]

136. Wei, S.; Di Lecce, D.; Brescia, R.; Pugliese, G.; Shearing, P.R.; Hassoun, J. Electrochemical behavior of nanostructured NiO@C anode in a lithium-ion battery using LiNi$_{1/3}$Co$_{1/3}$Mn$_{1/3}$O$_2$ cathode. *J. Alloys Compd.* **2020**, *844*, 155365. [CrossRef]

137. Ethiraj, A.S.; Uttam, P.; Varunkumar, K.; Chong, K.F.; Ali, G.A. Photocatalytic performance of a novel semiconductor nanocatalyst: Copper doped nickel oxide for phenol degradation. *Mater. Chem. Phys.* **2020**, *242*, 122520. [CrossRef]

138. Jayakumar, G.; Albert Irudayaraj, A.; Dhayal Raj, A. Photocatalytic Degradation of Methylene Blue by Nickel Oxide Nanoparticles. *Mater. Today Proc.* **2017**, *4*, 11690–11695. [CrossRef]

139. Khan, N.A.; Saeed, K.; Khan, I.; Gul, T.; Sadiq, M.; Uddin, A.; Zekker, I. Efficient photodegradation of orange II dye by nickel oxide nanoparticles and nanoclay supported nickel oxide nanocomposite. *Appl. Water Sci.* **2022**, *12*, 131. [CrossRef]

140. Barzinjy, A.A.; Hamad, S.M.; Aydın, S.; Ahmed, M.H.; Hussain, F.H.S. Green and eco-friendly synthesis of Nickel oxide nanoparticles and its photocatalytic activity for methyl orange degradation. *J. Mater. Sci. Mater. Electron.* **2020**, *31*, 11303–11316. [CrossRef]

141. Hamidian, K.; Rigi, A.H.; Najafidoust, A.; Sarani, M.; Miri, A. Study of photocatalytic activity of green synthesized nickel oxide nanoparticles in the degradation of acid orange 7 dye under visible light. *Bioprocess Biosyst. Eng.* **2021**, *44*, 2667–2678. [CrossRef]

142. Ahmed, B.; Kumar, S.; Ojha, A.K.; Donfack, P.; Materny, A. Facile and controlled synthesis of aligned WO$_3$ nanorods and nanosheets as an efficient photocatalyst material. *Spectrochim. Acta Part A Mol. Biomol. Spectrosc.* **2017**, *175*, 250–261. [CrossRef]

143. Mzimela, N.; Tichapondwa, S.; Chirwa, E. Visible-light-activated photocatalytic degradation of rhodamine B using WO$_3$ nanoparticles. *RSC Adv.* **2022**, *12*, 34652–34659. [CrossRef]

144. Acedo-Mendoza, A.; Infantes-Molina, A.; Vargas-Hernández, D.; Chávez-Sánchez, C.; Rodríguez-Castellón, E.; Tánori-Córdova, J. Photodegradation of methylene blue and methyl orange with CuO supported on ZnO photocatalysts: The effect of copper loading and reaction temperature. *Mater. Sci. Semicond. Process.* **2020**, *119*, 105257. [CrossRef]

145. Dong, P.; Hou, G.; Xi, X.; Shao, R.; Dong, F. WO$_3$-based photocatalysts: Morphology control, activity enhancement and multifunctional applications. *Environ. Sci. Nano* **2017**, *4*, 539–557. [CrossRef]

146. Ma, H.; Tsai, S.-B. Design of research on performance of a new iridium coordination compound for the detection of Hg2+. *Int. J. Environ. Res. Public Health* **2017**, *14*, 1232. [CrossRef] [PubMed]

147. Cao, Z.; Qin, M.; Jia, B.; Gu, Y.; Chen, P.; Volinsky, A.A.; Qu, X. One pot solution combustion synthesis of highly mesoporous hematite for photocatalysis. *Ceram. Int.* **2015**, *41*, 2806–2812. [CrossRef]

148. Yin, X.; Liu, L.; Ai, F. Enhanced Photocatalytic Degradation of Methylene Blue by WO$_3$ Nanoparticles Under NIR Light Irradiation. *Front. Chem.* **2021**, *9*, 683765. [CrossRef]

149. Tahir, M.; Nabi, G.; Hassan, A.; Iqbal, T.; Kiran, H.; Majid, A. Morphology tailored synthesis of C-WO 3 nanostructures and its photocatalytic application. *J. Inorg. Organomet. Polym. Mater.* **2018**, *28*, 738–745. [CrossRef]

150. Kumar, S.G.; Devi, L.G. Review on modified TiO$_2$ photocatalysis under UV/visible light: Selected results and related mechanisms on interfacial charge carrier transfer dynamics. *J. Phys. Chem. A* **2011**, *115*, 13211–13241. [CrossRef]